Effective-one-body multipolar waveforms for eccentric binary black holes with nonprecessing spins

Antoni Ramos-Buades,[1] Alessandra Buonanno,[1,2] Mohammed Khalil,[1,2] and Serguei Ossokine[1]

[1]*Max Planck Institute for Gravitational Physics (Albert Einstein Institute), Am Mühlenberg 1, Potsdam 14476, Germany*

[2]*Department of Physics, University of Maryland, College Park, Maryland 20742, USA*

(Received 16 December 2021; accepted 23 December 2021; published 17 February 2022)

We construct an inspiral-merger-ringdown eccentric gravitational-wave (GW) model for binary black holes with non-precessing spins within the effective-one-body formalism. This waveform model, `SEOBNRv4EHM`, extends the accurate quasi-circular `SEOBNRv4HM` model to eccentric binaries by including recently computed eccentric corrections up to 2PN order in the gravitational waveform modes, notably the $(l,|m|)=(2,2),(2,1),(3,3),(4,4),(5,5)$ multipoles. The waveform model reproduces the zero eccentricity limit with an accuracy comparable to the underlying quasicircular model, with the unfaithfulness of $\lesssim 1\%$ against quasicircular numerical-relativity (NR) simulations. When compared against 28 public eccentric NR simulations from the Simulating eXtreme Spacetimes catalog with initial orbital eccentricities up to $e \simeq 0.3$ and dimensionless spin magnitudes up to $+0.7$, the model provides unfaithfulness $< 1\%$, showing that both the $(2,|2|)$-modes and the higher-order modes are reliably described without calibration to NR datasets in the eccentric sector. The waveform model `SEOBNRv4EHM` is able to qualitatively reproduce the phenomenology of dynamical captures, and can be extended to include spin-precession effects. It can be employed for upcoming observing runs with the LIGO-Virgo-KAGRA detectors and used to re-analyze existing GW catalogs to infer the eccentricity parameters for binaries with $e \lesssim 0.3$ (at 20 Hz or lower) and spins up to $\lesssim 0.9$–0.95. The latter is a promising region of the parameter space where some astrophysical formation scenarios of binaries predict mild eccentricity in the ground-based detectors' bandwidth. Assessing the accuracy and robustness of the eccentric waveform model `SEOBNRv4EHM` for larger eccentricities and spins will require comparisons with, and, likely, calibration to eccentric NR waveforms in a larger region of the parameter space.

DOI: 10.1103/PhysRevD.105.044035

I. INTRODUCTION

Most inspiraling binaries observed by ground-based gravitational-wave (GW) detectors are likely to form via isolated binary evolution [1–14] and are expected to circularize [15] by the time they enter the detector frequency band. However, a small fraction of binaries may have non-negligible orbital eccentricity in the LIGO, Virgo or KAGRA [16–18] frequency band if they form through dynamical captures and interactions in dense stellar environments, such as globular clusters [19–39] or galactic nuclei [40–47], and through the Kozai-Lidov mechanism [48,49] in triple systems [50–56]. Thus, measuring eccentricity in the GW signal from merging binaries provides key information about the origin and the properties of the population of such binaries [57–62].

So far, the observed GW events detected by LIGO and Virgo [63–65] are consistent with quasicircular binary coalescences. Nevertheless, there are increasing efforts to search for eccentricity signatures in the current GW events [66–73]. With upcoming upgrades of ground-based detectors and third-generation detectors like the Einstein Telescope or the Cosmic Explorer [74–77], as well as future spaceborne detectors like LISA and TianQin [78,79], the fraction of GW events with non-negligible orbital eccentricity is expected to significantly increase [80–83]. Therefore, developing accurate waveform models that include the effects of eccentricity is essential to detect eccentric binaries, infer their properties, and provide information on their astrophysical origin.

Gravitational waveforms from inspiraling eccentric binaries have been developed within the post-Newtonian (PN) formalism [84–100]. Numerical-relativity (NR) simulations for eccentric binary black holes (BBHs) were produced in Refs. [70,101–106], but they are still limited to a small

region of the binary's parameter space and do not cover the entire bandwidth of ground-based detectors (unless the binary total mass is larger than $\sim 70\ M_\odot$ [106]). Under the assumption that the binary circularizes before merger, inspiral-merger-ringdown (IMR) (hybrid) waveforms, in time or frequency-domain, have been developed in Refs. [105,107,108] by combining the inspiral phase from PN with the merger and ringdown signal from either NR or the effective-one-body (EOB) formalism. Recently, NR surrogate models for equal-mass nonspinning eccentric binaries were built in Refs. [106] by directly interpolating NR simulations. Guided by comparisons with NR simulations, Ref. [109] has proposed a method to include eccentricity effects in existing quasicircular IMR waveform models for low eccentricity. Regarding systems with matter content, like binary neutron stars or neutron-star–black-hole binaries, there have been also efforts to produce eccentric NR simulations [110–112], as well as analytical work studying the coupling between eccentricity and tidal effects [113–115]. However, complete eccentric IMR waveform models including matter effects have not been developed, yet.

Within the efforts to model IMR waveforms for eccentric BBHs, the EOB formalism [116,117] has recently seen a lot of progress [118–127]. The EOB formalism is a framework that combines information from PN theory, NR and BH perturbation theory to accurately describe the inspiral, merger and ringdown of a binary coalescence (see e.g., Refs. [124,128–140]). The current eccentric EOB waveform models are constructed by improving the EOB description of the eccentric inspiral and plunge, but they still employ a quasicircular merger-ringdown model [121–124,127]. Nevertheless, this approach has been able to construct EOB waveforms that are faithful to existing, although limited, (public) NR waveforms from the Simulating eXtreme Spacetimes (SXS) catalog with eccentricity smaller than 0.3 and mild spins.

In this paper, we develop a multipolar eccentric EOB waveform model that builds on the quasicircular SEOBNRv4HM model [134] for BBHs with aligned spins[1] and includes recently derived eccentric corrections up to 2PN order [126], including spin-orbit and spin-spin interactions, in the $(l, |m|) = (2,2), (2,1), (3,3), (4,4), (5,5)$ multipoles. This eccentric waveform model, henceforth SEOBNRv4EHM, has comparable accuracy to the quasicircular SEOBNRv4HM model in the zero eccentricity limit when compared to quasicircular NR waveforms, and produces unfaithfulness $<1\%$ against eccentric NR simulations [107] from the SXS collaboration. When restricting to the $(2, |2|)$-modes we refer to the model as SEOBNRv4E, in analogy to the quasicircular case, which corresponds to the SEOBNRv4 model in Ref. [132]. Furthermore, we develop generic initial conditions for elliptical orbits including two eccentric parameters. We also implement hyperbolic-orbit initial conditions, and we briefly show the ability of the model to reproduce the phenomenology of hyperbolic encounters, thus paving the path to the description of generic BBH coalescences.

This paper is structured as follows. In Sec. II, we outline our multipolar eccentric EOB waveforms, and describe how the eccentricity effects are introduced in each building block of the model, notably the conservative and dissipative dynamics and the gravitational waveform modes. We also develop initial conditions for elliptic orbits including two eccentric parameters. In Sec. III, we assess the accuracy of the multipolar eccentric waveform model by comparing it against 141 NR waveforms in the quasicircular limit, and to 28 public eccentric NR waveforms from the SXS waveform catalog [141,142]. We develop an algorithm to estimate the best matching parameters between the eccentric EOB and NR waveforms, analyze the robustness of the model across parameter space and start to estimate for which source's parameters and eccentricity, we could anticipate biases in inference studies if quasicircular-orbit waveforms were used. In Sec. IV, we summarize our main conclusions and discuss future work. Finally, in Appendix A we list the eccentric corrections to the waveform modes obtained in Ref. [126], in Appendix B we describe details of the implementation of the eccentric waveforms modes, and in Appendix C we provide the expressions of the dynamical quantities needed for calculating the initial conditions for eccentric orbits.

In this paper, we use geometric units, setting $G = c = 1$ unless otherwise specified.

II. ECCENTRIC EFFECTIVE-ONE-BODY WAVEFORM MODEL

Here, we develop the multipolar eccentric aligned-spin SEOBNRv4EHM waveform model building on the quasicircular aligned-spin SEOBNRv4HM model [134], which has been used by LIGO and Virgo to detect GW signals and infer binary properties [63–65]. More specifically, we provide a brief description of the (conservative) dynamics in Sec. II A, waveform modes in Sec. II B, and initial conditions in Sec. II C.

The EOB formalism maps the two-body dynamics of objects with masses m_i and spins $\boldsymbol{S}_i$, with $i = 1, 2$, into an effective dynamics of a test-spin with mass $\mu = m_1 m_2/(m_1 + m_2)$ and spin $\boldsymbol{S}_*$ moving in a deformed Kerr metric with mass $M = m_1 + m_2$ and spin $\boldsymbol{S}_{\rm Kerr}$. The deformation parameter is the (dimensionless) symmetric mass ratio $\nu = \mu/M$. As we are limiting to spins aligned to the orbital angular momentum, the only (dimensionless) spin component on which the dynamics and the waveform depend is $\chi_i = \boldsymbol{S}_i \cdot \hat{\boldsymbol{L}}/m_i^2$, where $\hat{\boldsymbol{L}}$ is the unit vector in the direction perpendicular to the orbital plane.

[1]To ease the notation we use the term aligned spins when referring to aligned/anti-aligned spins.

A. Effective-one-body dynamics

The EOB conservative dynamics is governed by the EOB Hamiltonian, calculated from the effective Hamiltonian through the energy map [116]

$$H_{\rm EOB} = M\sqrt{1+2\nu\left(\frac{H_{\rm eff}}{\mu}-1\right)}. \tag{1}$$

When both spins are aligned with the orbital angular momentum, the motion is restricted to a plane. This implies that the dynamical variables entering the Hamiltonian are the (dimensionless) radial separation $r \equiv R/M$, the orbital phase ϕ, and their (dimensionless) conjugate momenta $p_r \equiv P_r/\mu$ and $p_\phi \equiv P_\phi/\mu$. We use the same effective Hamiltonian, $H_{\rm eff}$, as described in Refs. [131,143], augmented with the parameters $(K, d_{\rm SO}, d_{\rm SS}, \Delta t^{22}_{\rm peak})$ calibrated to NR waveforms from Ref. [132].

The dissipative dynamics within the EOB formalism is described by a radiation-reaction (RR) force $\mathcal{F}$, which enters the Hamilton equations of motion, as [130,144]

$$\begin{aligned}
\dot{r} &= \xi(r)\frac{\partial \hat{H}_{\rm EOB}}{\partial p_{r_*}}(r, p_{r_*}, p_\phi),\\
\dot{\phi} &= \frac{\partial \hat{H}_{\rm EOB}}{\partial p_\phi}(r, p_{r_*}, p_\phi),\\
\dot{p}_{r_*} &= -\xi(r)\frac{\partial \hat{H}_{\rm EOB}}{\partial r}(r, p_{r_*}, p_\phi) + \hat{\mathcal{F}}_r,\\
\dot{p}_\phi &= \hat{\mathcal{F}}_\phi,
\end{aligned} \tag{2}$$

where the dot represents the time derivative $d/d\hat{t}$, with respect to the dimensionless time $\hat{t} \equiv T/M$, $\hat{H}_{\rm EOB} \equiv H_{\rm EOB}/\mu$, and $\hat{\mathcal{F}}_\phi \equiv \mathcal{F}_\phi/M$. The equations are expressed in terms of $p_{r_*} \equiv p_r\xi(r)$, which is the conjugate momentum to the tortoise-coordinate r_*, and $\xi(r) \equiv dr/dr_*$ can be expressed in terms of the potentials of the effective Hamiltonian [144].

In the case of the SEOBNRv4HM waveform model, the components of the RR force are computed using the following relations [117,145]

$$\hat{\mathcal{F}}_\phi = -\frac{\Phi_E}{\omega}, \qquad \hat{\mathcal{F}}_r = \hat{\mathcal{F}}_\phi\frac{p_r}{p_\phi}, \tag{3}$$

where $\omega = \dot{\phi}$ is the (dimensionless) orbital frequency, and Φ_E is the energy flux for quasicircular orbits written as a sum over waveform modes using [128,129]

$$\Phi_E = \frac{\omega^2}{16\pi}\sum_{l=2}^{8}\sum_{m=-l}^{l} m^2\left|\frac{D_L}{M}h_{lm}\right|^2, \tag{4}$$

where D_L is the luminosity distance between the binary system and the observer. The above relation is only valid for quasicircular orbits as it assumes the relation between energy and angular-momentum fluxes $\Phi_E = \omega\Phi_J$, which is only valid for quasicircular orbits.

We note that in the SEOBNRv4HM model, eccentric effects are already partially included in the radial component of the RR force $\hat{\mathcal{F}}_r$ since it is proportional to p_r, whereas the tangential component of the RR force $\hat{\mathcal{F}}_\phi$ does not contain eccentric corrections. Recently, Ref. [126] derived the eccentric corrections of the RR force up to 2PN order, including spin-orbit and spin-spin interactions, in a factorized form [128,129]. We have explored adding those corrections to both components of the RR force in the SEOBNRv4HM model. However, we find, when doing it, that the late-inspiral dynamics can lead to differences with respect to the one of the SEOBNRv4HM model, affecting the inclusion of the merger-ringdown signal that is inherited from the SEOBNRv4HM model. This in turn, can lead to differences between our new model and SEOBNRv4HM in the quasicircular orbit limit, and, for some binary configurations, to the degradation of the model performance when compared to quasicircular NR simulations. Since the goal of this paper is to develop an eccentric waveform model that reduces to the SEOBNRv4HM model in the quasicircular limit and is faithful to the current (public) SXS NR eccentric waveforms (which have eccentricity smaller than 0.3), we choose to retain the conservative and dissipative dynamics of the SEOBNRv4HM model and introduce the eccentric corrections of Ref. [126] only in the gravitational modes. The latter are not used to compute the fluxes employed to construct the RR force. We leave the inclusion of the eccentric corrections to the RR force for the next generation of EOBNR models [146], which will be recalibrated to quasicircular NR simulations.[2]

B. Effective-one-body gravitational waveforms

As in previous EOBNR models, we represent the inspiral-plunge signal of the SEOBNRv4EHM waveforms as:

$$h^{\rm insp\text{-}plunge}_{lm} = h^{\rm ecc}_{lm}N_{lm}, \tag{5}$$

where the $h^{\rm ecc}_{lm}$'s are the factorized EOB gravitational modes [128,129], including the 2PN eccentric corrections derived in Ref. [126], while the N_{lm}'s are the so-called nonquasicircular (NQC) terms. More specifically, the $h^{\rm ecc}_{lm}$ terms are written as:

$$h^{\rm ecc}_{lm} = h^{\rm N}_{lm}S_{\rm eff}(T^{\rm qc}_{lm} + T^{\rm ecc}_{lm})(f^{\rm qc}_{lm} + f^{\rm ecc}_{lm})e^{i\delta_{lm}}, \tag{6}$$

[2]The quasicircular TEOBResumS model [133] does not include the radial component of the RR force $\hat{\mathcal{F}}_r$, but its extension to eccentric orbits [123] includes a nonzero $\hat{\mathcal{F}}_r$ that is linear in p_r, adds eccentric corrections at Newtonian order in $\hat{\mathcal{F}}_\phi$, and is recalibrated to NR waveforms in the quasicircular orbit limit.

where $h^{\rm N}_{lm}$ is the Newtonian (leading-order) quasicircular (qc) term, $S_{\rm eff}$ is an effective source term, $T^{\rm qc}_{lm}$ resums the leading logarithms in the tail effects, while δ_{lm} contains phase corrections, and $f^{\rm qc}_{lm}$ ensures that the PN expansion of $h^{\rm qc}_{lm}$ agrees with the PN expressions for the modes in the quasicircular orbit limit. The explicit expressions for the above terms can be found in Refs. [129,132,134,147]. Furthermore, the term $T^{\rm ecc}_{lm}$ includes eccentric corrections to the leading-order hereditary part, while $f^{\rm ecc}_{lm}$ contains the eccentric corrections to the 2PN instantaneous part, including the Newtonian (leading-order) term. Note that the eccentric corrections are not introduced in $\delta_{\ell m}$. We note that the eccentric-orbit terms are provided in the Supplemental Material of Ref. [126], and for completeness, we write them in Appendix A for the $(l,|m|) = \{(2,2),(2,1),(3,3),(4,4),(5,5)\}$ modes.

We use the same expression of the NQC correction as in the `SEOBNRv4HM` model, that is [132,134]

$$N_{lm} = \left[1 + \frac{p^2_{r_*}}{(r\omega)^2}\left(a^{lm}_1 + \frac{a^{lm}_2}{r} + \frac{a^{lm}_3}{r^{3/2}}\right)\right] \times \exp\left[i\left(b^{lm}_1 \frac{p_{r_*}}{r\omega} + b^{lm}_2 \frac{p^3_{r_*}}{r\omega}\right)\right], \tag{7}$$

where the coefficients $(a^{lm}_1, a^{lm}_2, a^{lm}_3, b^{lm}_1, b^{lm}_2)$ are fixed by requiring that the amplitude, its first and second derivatives, as well as the GW frequency and its first derivative agree for every (l,m)-mode with values extracted from NR waveforms [134] (i.e., the NR input values). However, as we shall discuss below, we orbit-average the NQC corrections (7) in the eccentric `SEOBNRv4HM` waveform model.

Both the eccentric corrections to the waveform and the NQC terms are designed to improve the accuracy of the EOB waveforms. However, we find that modifications to both have to be introduced in order to improve the faithfulness of the EOB model to NR simulations. The eccentric corrections to the modes are derived from PN and EOB theory, thus they increase the accuracy of the inspiral part of the eccentric model. Nonetheless, in the strong-field regime, very close to the merger-ringdown attachment time [132,134], we found that they can lead to high unfaithfulness with respect to NR waveforms. This is due to the fact that they can modify by orders of magnitude the NR input values (in particular the amplitude, frequency and their derivatives) used to compute the coefficients in the NQC terms. To mitigate this effect, we introduce a sigmoid function that makes the eccentric corrections, $f^{\rm ecc}_{lm}$ and $T^{\rm ecc}_{lm}$, vanish at merger,

$$w(\beta, t_\beta; t) = \frac{1}{1 + e^{-\beta(t - t_\beta)}}, \tag{8}$$

where we choose $\beta = 0.09$ and $t_\beta \equiv t^{\omega}_{\rm peak} - 300$, being $t^{\omega}_{\rm peak}$ the time when the peak of $\omega \equiv \dot{\phi}$ occurs.

Moreover, the NQC corrections to the waveform defined in Eq. (7) become highly oscillatory during an eccentric inspiral, as all the dynamical quantities composing its ansatz have increasing oscillations with increasing eccentricity. One approach to circumvent the oscillatory behavior of the NQC function is the application of a window function [122–124,127], like the sigmoid in Eq. (8), close to merger. This window function forces the NQC function to approach unity during the inspiral, and have significant effects only near merger.

Here we develop an alternative approach, which consists in orbit averaging the dynamical quantities entering the ansatz of the NQC corrections, so that it is a monotonic function during the whole evolution. The rationale is that the genuine oscillations due to the orbital eccentricity are already included in Eq. (6), thus the role of the NQC corrections is merely to improve the GW amplitude and frequency of the EOB model during plunge and merger using inputs from NR.

Any dynamical quantity $X(t)$ can be orbit-averaged at the ith-orbit passage as follows,

$$\bar{X}_i = \frac{1}{t_{i+1} - t_i}\int_{t_i}^{t_{i+1}} X_i(t)dt, \tag{9}$$

where (t_i, t_{i+1}) correspond to times defining the complete orbits. We note that in order to perform the orbit average calculation, we need to identify the times, t_i, which define successive orbits. In practice, we can choose either the maxima or the minima of any orbital quantity to identify the orbits. In the case of the orbital separation, these times correspond to the turning points, either apastron or periastron passages. We decide to use the time of the maxima to perform the orbit average in Eq. (9), and we associate each orbit average value to an intermediate time defined as $\bar{t}_i = (t_{i+1} + t_i)/2$ [103]. From Eq. (7) it can be seen that the dynamical quantities entering the NQC corrections are $r(t)$, $p_{r_*}(t)$ and $\omega(t)$. Thus, the NQC corrections implemented in the model can be expressed in terms of the orbit-average quantities as,

$$\bar{N}_{lm} = \left[1 + \frac{\bar{p}^2_{r_*}}{\bar{r}^2\bar{\omega}^2}\left(a^{lm}_1 + \frac{a^{lm}_2}{\bar{r}} + \frac{a^{lm}_3}{\bar{r}^{3/2}}\right)\right] \times \exp\left[i\left(b^{lm}_1 \frac{\bar{p}_{r_*}}{\bar{r}\,\bar{\omega}} + b^{lm}_2 \frac{\bar{p}^3_{r_*}}{\bar{r}\,\bar{\omega}}\right)\right], \tag{10}$$

where the coefficients $(a^{lm}_1, a^{lm}_2, a^{lm}_3, b^{lm}_1, b^{lm}_2)$ are computed as in Eq. (7). Hence, the modes in `SEOBNRv4EHM` can be expressed as follows,

$$\bar{h}^{\rm insp\text{-}plunge}_{lm} = h^{\rm N}_{lm} S_{\rm eff} T_{lm} f_{lm} e^{i\delta_{lm}} \bar{N}_{lm}, \tag{11}$$

$$T_{lm} = T^{\rm qc}_{lm} + [1 - w(\beta, t_\beta; t)]T^{\rm ecc}_{lm}, \tag{12}$$

$$f_{lm} = f^{\rm qc}_{lm} + [1 - w(\beta, t_\beta; t)]f^{\rm ecc}_{lm}. \tag{13}$$

where the NQC terms $\bar{N}_{lm}$ are given by Eq. (10). The full details of the orbit averaging procedure can be found in the Appendix B.

The procedure described above ensures that during an eccentric inspiral there are no unphysical oscillations coming from the oscillatory nature of the dynamical variables in the NQC correction, while the windowing applied to the eccentric terms close to merger ensures that the circularization hypothesis at merger is fulfilled, making the input values of the eccentric model closer to the ones of the underlying quasicircular model. In Sec. III D, we quantify the validity in parameter space of the approximations used to treat the NQC corrections. Furthermore, in Secs. III B and III C, we show that this procedure provides a quasicircular limit with an accuracy comparable to the underlying quasicircular SEOBNRv4HM model, and a high faithfulness when compared to eccentric NR simulations.

C. Eccentric initial conditions

We now complete the eccentric waveform model with the specification of the initial conditions for elliptical orbits and hyperbolic orbits.

The gravitational signal emitted by an aligned-spin eccentric BBH system is described by 6 intrinsic parameters: the component masses m_1 and m_2 (or equivalently mass ratio $q = m_1/m_2$ and total mass $M = m_1 + m_2$), the dimensionless spin components χ_1 and χ_2 introduced at the beginning of Sec. II, the orbital eccentricity e, and a radial phase parameter ζ. For the parameter describing the position of a point on an ellipse, several options with different physical meaning are possible: mean anomaly, relativistic anomaly, true anomaly, etc.. Here, we adopt the relativistic anomaly. In general relativity, for BBH systems, the total mass is just a scale parameter that can be set to 1. Thus, the initial conditions for the EOB evolution of the SEOBNRv4EHM model depend only on 5 parameters, which have to be specified at a certain starting frequency ω_0.

Since the eccentricity parameter e is gauge dependent, we can choose a measure of the eccentricity that is as convenient as possible for the numerical implementation. The only requirement is that, in the zero eccentricity limit, we recover the quasicircular initial conditions [145] used in the SEOBNRv4HM model. Reference [126] derived such initial conditions for eccentric orbits assuming the periastron as the starting point. Here, we generalize those initial conditions to start from an arbitrary point on the orbit, thus making the eccentric initial conditions depend on both e and ζ.

We use the eccentricity e defined in the Keplerian parametrization of the orbit

$$r = \frac{1}{u_p(1 + e\cos\zeta)}, \tag{14}$$

where u_p is the inverse semilatus rectum, and ζ the relativistic anomaly, which equals 0 at periastron and π at apastron. Given the initial orbital frequency ω_0, eccentricity e_0, relativistic anomaly ζ_0, masses, and spins, we obtain the initial conditions for r_0 and $p_{\phi 0}$ in absence of radiation reaction by solving the following equations:

$$\left[\frac{\partial \hat{H}_{\rm EOB}}{\partial r}\right]_0 = -[\dot{p}_r(p_\phi, e, \zeta)]_0, \qquad \left[\frac{\partial \hat{H}_{\rm EOB}}{\partial p_\phi}\right]_0 = \omega_0, \tag{15}$$

with $p_r(p_\phi, e, \zeta)$ and $\dot{p}_r(p_\phi, e, \zeta)$ given by the 2PN-order expressions given in Eqs. (C3) and (C4) of the Appendix C.

Using the solution for r_0 and $p_{\phi 0}$, we obtain the initial condition for p_{r_0} by numerically solving

$$\left[\frac{\partial \hat{H}_{\rm EOB}}{\partial p_r}\right]_0 = [\dot{r}^{(0)} + \dot{r}^{(1)}]_0, \tag{16}$$

where $\dot{r}^{(0)}$ is the 2PN-order expression for $\dot{r}$ at zeroth order in the RR effects (see Eq. (C5), while $\dot{r}^{(1)}$ is the first-order term in the RR part of $\dot{r}$, for which we use the quasicircular expression derived in Ref. [145]

$$\dot{r}^{(1)} = -\frac{\Phi_E^{\rm qc}}{\omega}\frac{\partial^2 \hat{H}_{\rm EOB}/\partial r \partial p_\phi}{\partial^2 \hat{H}_{\rm EOB}/\partial r^2}, \tag{17}$$

being $\Phi_E^{\rm qc}$ the quasicircular energy flux given in Eq. (4). Finally, the initial value p_{r_0} is converted into the tortoise-coordinate conjugate momentum $p_{r_{*0}}$, using the relations in Sec. II A, so that together with r_0 and $p_{\phi 0}$, it can be introduced in Eqs. (2) to evolve the EOB equations of motion.

It is worthwhile to compare our initial orbital eccentricity $e_0^{\rm IC}$, with the eccentricity measured directly from the orbital frequency, $e_{\omega_{\rm orb}}$, and the eccentricity computed from the frequency of the (2, 2) mode, $e_{\omega_{22}}$, by using the following eccentricity estimator [105,148]

$$e_\omega = \frac{\omega_p^{1/2} - \omega_a^{1/2}}{\omega_p^{1/2} + \omega_a^{1/2}}, \tag{18}$$

where ω_a and ω_p correspond to the frequency, either the orbital or (2, 2)-mode frequency, at apastron and periastron, respectively.

Starting at periastron ($\zeta = 0$), we produce a sample of 5×10^5 points randomly distributed in the parameter space $q \in [1, 20]$, $\chi_{1,2} \in [-0.9, 0.9]$ and $e_0^{\rm IC} \in [0.01, 0.3]$, and compute the relative difference between $e_{\rm IC}^0$ and $e_{\omega_{22}}^0$ or $e_{\omega_{\rm orb}}^0$. In the upper panel of Fig. 1, we show the relative difference between $e_0^{\rm IC}$ and $e_{\omega_{22}}^0$ for some nonspinning configurations with mass ratios $q = \{1, 4, 8, 10, 15, 20\}$. For the same cases we show in the inset of Fig. 1 the relative difference between $e_{\rm IC}^0$ and $e_{\omega_{\rm orb}}^0$. We observe that

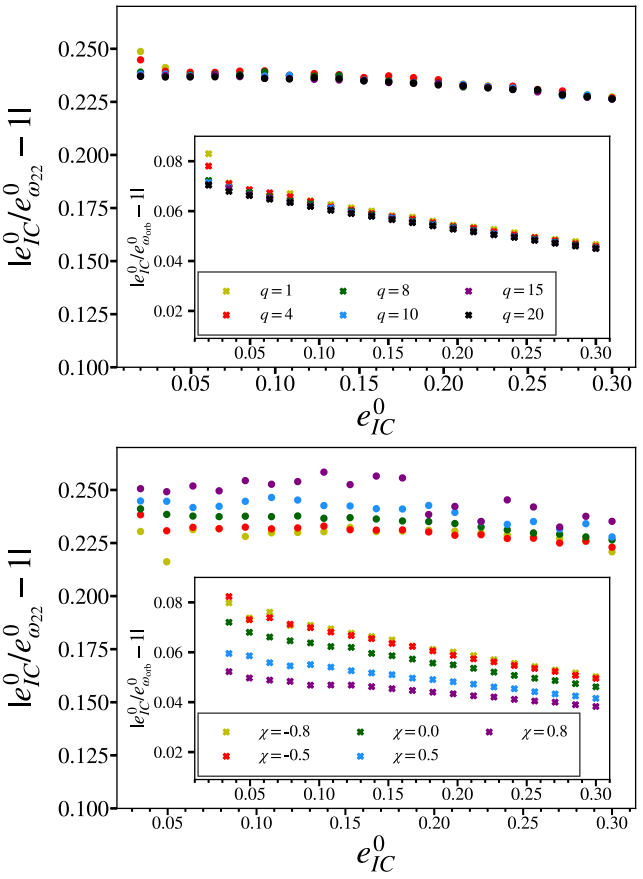

FIG. 1. Top panel: relative difference between the initial eccentricity from the initial conditions of SEOBNRv4EHM, $e^0_{\rm IC}$, and the initial eccentricity computed from the frequency of the (2, 2) mode, $e^0_{\omega_{22}}$, of SEOBNRv4EHM as a function of $e^0_{\rm IC}$ in the range [0.02, 0.3] for nonspinning configurations with mass ratios $q = \{1, 4, 8, 10, 15, 20\}$. Lower panel: same quantity as in the upper panel for a configuration with fixed mass ratio $q = 2$, same range of $e^0_{\rm IC}$, and distinct equal-spin values $\chi_1 = \chi_2 = \{-0.8, -0.5, 0, 0.5, 0.8\}$. The insets of both panels show the relative difference between $e^0_{\rm IC}$ and the eccentricity measured from the orbital frequency of SEOBNRv4EHM $e^0_{\omega_{\rm orb}}$, for the same configurations as in the larger panels.

the relative difference for $e^0_{\omega_{22}}$ is ∼24%, while for $e^0_{\omega_{\rm orb}}$ is significantly lower ∼6%. Moreover, the dependence on mass ratio is smaller than 1%, in relative difference, with the exception of the lower eccentricity cases where the measurement of the eccentricity has also a larger error, which we estimate to be ∼3%. We also note that with increasing values of $e^0_{\rm IC}$ the relative differences decrease, especially for the eccentricity measured from the orbital frequency.

In the lower panel of Fig. 1, we fix the mass ratio $q = 2$, and vary the spin values $\chi_1 = \chi_2 = \{-0.8, -0.5, 0, 0.5, 0.8\}$ for the same range of initial eccentricities as in the upper panel. The results show that the relative error between $e^0_{\omega_{22}}$ and $e^0_{\rm IC}$ is $\sim 22 - 25\%$ when varying the spin values. These variations are quite similar to the results obtained when varying the mass ratios. The relative error between $e^0_{\omega_{\rm orb}}$ and $e^0_{\rm IC}$ is $\sim 5 - 8\%$, which is also very close in magnitude to the nonspinning case. However, in the lower panel of Fig. 1, one can appreciate that the relative errors vary more with spins than with mass ratio, specifically for positive spins the relative errors with respect to $e^0_{\omega_{22}}$ are $1 - 2\%$ larger than for negative spins, while the relative errors for $e^0_{\omega_{\rm orb}}$ follow the inverse dependence with spins.

When considering the larger dataset of 5×10^5 configurations, we find that the relative error between $e^{\rm IC}_0$ and $e^0_{\omega_{22}}$ has an average of ∼30% error, with the largest difference of 40% for low eccentricities, where the errors in measuring the eccentricity are also larger due to the difficulties in determining the maxima and minima. For the relative error between $e^{\rm IC}_0$ and $e^0_{\omega_{\rm orb}}$, the average value is ∼6%, reaching up to ∼14% for low values of the eccentricities. The results show a better agreement between $e^0_{\rm IC}$ and $e^0_{\omega_{\rm orb}}$ than between $e^0_{\rm IC}$ and $e^0_{\omega_{22}}$. The relation between these different definitions of eccentricity can be derived using PN theory, and it will be presented in future work [149].

We note that the results reported in Fig. 1 quantify differences between the eccentricity specified in the SEOBNRv4EHM model and two other possible definitions of the eccentricity. We remark that even though there is no unique definition of the eccentricity, this kind of quantitative analysis will be required in future parameter-estimation analysis of eccentric GW sources with the LIGO, Virgo and KAGRA detectors in order to reliably compare the results among different eccentric waveform models.

Finally, we have also implemented hyperbolic-orbit initial conditions for the SEOBNRv4EHM model. The hyperbolic initial conditions are specified by the initial energy E_0 and angular momentum $p_{\phi 0}$ at infinity, which in practice we take at an initial orbital separation $r_0 = 10^4 M$. We fix a value of the angular momentum p_{ϕ_0}, and choose a value of the initial energy E_0/M. The choice of E_0/M is typically done between the energy with zero radial momentum $E_{\rm min} = H_{\rm EOB}(r_0, p_{\phi 0}, p_{r_{*}0} = 0)$ and the energy at the last stable circular orbit (LSO) $E_{\rm max} = H_{\rm EOB}(r_{\rm LSO}, p_\phi{}^{\rm LSO}, p^{\rm LSO}_{r^*})$ [150–152]. Then, we solve the following equation for $p_{r_{*0}}$,

$$E_0 \equiv H_{\rm EOB}(r_0, p_{\phi 0}, p_{r_{*}0}). \tag{19}$$

This procedure to set the initial conditions for hyperbolic orbits is very similar to the one used in the literature [150,151], although we note that others are possible, for instance, one could express the initial conditions in terms of the initial velocity and impact parameter [153–155]. In Fig. 2, we show the trajectory of a dynamical capture, as well as, the real part of the different multipoles in the SEOBNRv4EHM model. Although the model is able to reproduce the behavior of dynamical captures and hyperbolic encounters, we focus in this paper on the eccentric

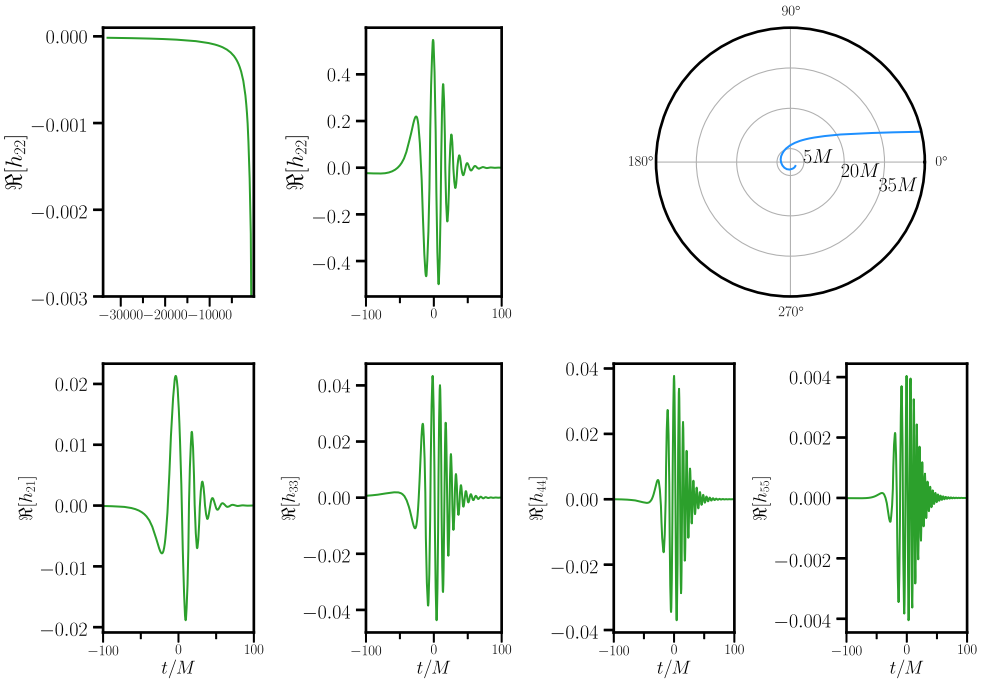

FIG. 2. Waveform characteristics for a mass ratio $q = 1.5$ nonspinning configuration with initial parameters $r_0 = 10^4M$, $p_{\phi 0} = 3.97$ and $E_0/M = 1.012$. Top row: from left to right, the two first panels show the real part of the 22-mode waveform in time domain, the first plot displays the full domain of the waveform while the second one zooms in into the merger part. The third panel displays the trajectory $r(\varphi)$ in polar coordinates. Each circle corresponds to a constant value of the orbital separation, which is marked on the figure. Bottom row: from left to right, the real part of the (2, 1), (3, 3), (4, 4), (5, 5) modes in time domain zooming in close to the merger and ringdown regions.

bound orbit case, and leave a thorough and quantitative analysis of the hyperbolic orbits, including comparison to NR results to the future.

III. PERFORMANCE OF THE MULTIPOLAR ECCENTRIC EFFECTIVE-ONE-BODY WAVEFORM MODEL

In this section, we first assess the accuracy of the multipolar eccentric waveform model `SEOBNRv4EHM` against the quasicircular and eccentric NR waveforms at our disposal, using the faithfulness function, which is a metric introduced to quantify the closeness of two waveforms. Then, we explore the robustness and validity of the `SEOBNRv4EHM` model in the region of parameter space where we do not yet have NR waveforms. Finally, we evaluate the unfaithfulness between IMR eccentric waveforms and quasicircular ones to estimate in which part of the parameter space and for which values of the eccentricity we expect large biases in recovering the source's properties if quasicircular orbit waveforms were used.

A. Faithfulness function

The GW signal emitted by an eccentric aligned-spin BBH system depends on 13 parameters. In Sec. II C, we have introduced the 6 intrinsic parameters describing the source properties of such a system. There are 7 additional parameters which relate the source and detector frames, notably the angular position of the line of sight measured in the source frame (ι, φ_0), the sky location of the source in the detector frame (θ, ϕ), the polarization angle ψ, the luminosity distance of the source D_L and the time of arrival t_c.

The signal measured by the detector takes the form:

$$h(t) = F_+(\theta,\phi,\psi)h_+(\iota,\varphi_0,D_L,\mathbf{\Theta},t_c;t) + F_\times(\theta,\phi,\psi)h_\times(\iota,\varphi_0,D_L,\mathbf{\Theta},t_c;t), \quad (20)$$

where $\mathbf{\Theta} = \{m_{1,2},\chi_{1,2},e,\zeta\}$, and $F_+(\theta,\phi,\psi)$ and $F_\times(\theta,\phi,\psi)$ are the antenna-pattern functions [156,157]. Equation (20) can be written in terms of an effective polarization angle $\kappa(\theta,\phi,\psi)$ as

$$h(t) = \mathcal{A}(\theta,\phi)[h_+\cos\kappa + h_+\sin\kappa], \quad (21)$$

where the definition of $\mathcal{A}(\theta,\phi)$ can be found in Refs. [134,137], and we have removed the dependences of κ, h_+ and $h_\times$ to ease the notation. The GW polarizations can be decomposed as

$$h_+ - ih_\times = \sum_{l=2}^{\infty}\sum_{m=-l}^{m=+l} {}_{-2}Y_{lm}(\varphi,\iota)h_{lm}(\mathbf{\Theta};t), \quad (22)$$

where $h_{lm}(\mathbf{\Theta};t)$ represents the gravitational waveform modes, and $Y^{-2}_{lm}(\varphi,\iota)$ are the -2 spin-weighted spherical harmonics.

We introduce the inner product between two waveforms h_1 and h_2 [156,157] as

$$\langle h_1|h_2\rangle = 4\Re\int_{f_{\rm min}}^{f_{\rm max}}\frac{\hat{h}_1(f)\hat{h}_2^*(f)}{S_n(f)}df, \tag{23}$$

where the star denotes complex conjugate, the hat the Fourier transform, and $S_n(f)$ is the one-sided power-spectral density (PSD) of the detector noise. In this work we use the Advanced LIGO's zero-detuned high-power design sensitivity curve [158]. When both waveforms are in band, we use $f_{\rm min}=10$ Hz and $f_{\rm max}=2048$ Hz, as the lower and upper bounds of the integral. For NR waveforms where this is not the case, we set $f_{\rm min}=1.05f_{\rm start}$, where $f_{\rm start}$ is the starting frequency of the NR waveform.

The agreement between two waveforms—for example, the signal, h_s, and the template, h_t, observed by a detector, can be assessed by computing the faithfulness function [134,137],

$$\mathcal{F}(M_{\rm s},\iota_{\rm s},\varphi_{0{\rm s}},\kappa_{\rm s})=\max_{t_c,\varphi_{0t},\kappa_t}\left[\frac{\langle h_s|h_t\rangle}{\sqrt{\langle h_s|h_s\rangle\langle h_t|h_t\rangle}}\bigg|_{\substack{\iota_{\rm s}=\iota_t\\ \mathbf{\Theta}_{\rm s}(t_{\rm s}=t_{0_{\rm s}})=\mathbf{\Theta}_t(t_t=t_{0_t})}}\right]. \tag{24}$$

In Eq. (24) the inclination angle of the signal and the template are set to be the same, while the coalescence time, azimuthal angle and effective polarization angle of the template $(t_{0_t},\varphi_{0_t},\kappa_t)$, are adjusted to maximize the faithfulness of the template. This is a typical choice made when comparing waveforms with higher-order modes [134,137,159]. It is convenient to introduce the *sky-and-polarization averaged faithfulness* to reduce the dimensionality of the faithfulness function and express it in a more compact form [134,137],

$$\bar{\mathcal{F}}(M_{\rm s})=\frac{1}{8\pi^2}\int_{-1}^{1}d(\cos\iota_{\rm s})\int_0^{2\pi}d\varphi_{0{\rm s}}\int_0^{2\pi}d\kappa_{\rm s}\mathcal{F}(M_{\rm s},\iota_{\rm s},\varphi_{0{\rm s}},\kappa_{\rm s}). \tag{25}$$

Another useful metric to assess the closeness between waveforms is the signal-to-noise (SNR)-weighted faithfulness [137]

$$\bar{\mathcal{F}}_{\rm SNR}(M_{\rm s})=\sqrt[3]{\frac{\int_{-1}^{1}d(\cos\iota_{\rm s})\int_0^{2\pi}d\kappa_{\rm s}\int_0^{2\pi}d\varphi_{0{\rm s}}\mathcal{F}^3(M_{\rm s},\iota_{\rm s},\varphi_{0{\rm s}},\kappa_{\rm s}){\rm SNR}^3(\iota_{\rm s},\varphi_{0{\rm s}},\kappa_{\rm s})}{\int_{-1}^{1}d(\cos\iota_{\rm s})\int_0^{2\pi}d\kappa_{\rm s}\int_0^{2\pi}d\varphi_{0{\rm s}}{\rm SNR}^3(\iota_{\rm s},\varphi_{0{\rm s}},\kappa_{\rm s})}}, \tag{26}$$

where the SNR is defined as

$${\rm SNR}(\iota_{\rm s},\varphi_{0{\rm s}},\theta_{\rm s},\phi_{\rm s},\kappa_{\rm s},D_{\rm Ls},\mathbf{\Theta}_{\rm s},t_{cs})\equiv\sqrt{(h_{\rm s},h_{\rm s})}. \tag{27}$$

In Eq. (26) the weighting by the SNR takes into account the dependence on the phase and effective polarization of the signal at a fixed distance. Finally, we introduce the unfaithfulness or mismatch as

$$\bar{\mathcal{M}}=1-\bar{\mathcal{F}}. \tag{28}$$

B. Comparison against quasicircular numerical-relativity waveforms

We begin by assessing the accuracy of the SEOBNRv4EHM waveform model in the zero eccentricity limit, focusing on the unfaithfulness against the set of quasicircular NR waveforms used to calibrate and validate the SEOBNRv4HM model. The public NR waveforms are available in the SXS waveform catalog [141] produced with the spectral Einstein code (SPEC) [160]. The parameters of the public and nonpublic 141 NR waveforms are listed in the Appendix F of Ref. [134].

In order to simplify our analysis, we restrict first to the $(2,|2|)$-modes waveforms, and then include higher order modes. For the dominant $(2,|2|)$-modes the faithfulness can be simplified with respect to Eq. (24) as the inclination angle of the signal is not usually considered due to the angular dependence of the ${}_{-2}Y_{2\pm2}$ harmonics, and the fact that κ, ι and φ are degenerate [161]. Therefore, the faithfulness function for the quasicircular $(2,|2|)$-modes waveforms can be expressed as

$$\mathcal{F}_{22}(M_{\rm s},\varphi_{0{\rm s}})=\max_{t_c,\varphi_{0t}}\left[\frac{\langle h_s|h_t\rangle}{\sqrt{\langle h_s|h_s\rangle\langle h_t|h_t\rangle}}\bigg|_{\mathbf{\Theta}_{\rm s}(t_{\rm s}=t_{0_{\rm s}})=\mathbf{\Theta}_t(t_t=t_{0_t})}\right]. \tag{29}$$

In practice, we remove the dependence of the faithfulness on the azimuthal angle of the signal by evaluating Eq. (29) in a grid of 8 values for $\varphi_{0{\rm s}}\in[0,2\pi]$, and averaging the result to obtain $\bar{\mathcal{F}}_{22}$. The optimization over the coalescence time of the signal is efficiently computed by applying an inverse Fourier transform [162] and we analytically optimize over the coalescence phase of the template [161]. From Eq. (29) one can define the mismatch or unfaithfulness as,

$$\bar{\mathcal{M}}_{22} = 1 - \bar{\mathcal{F}}_{22}. \tag{30}$$

The condition $\mathbf{\Theta}_s(t_s = t_{0_s}) = \mathbf{\Theta}_t(t_t = t_{0_t})$ in Eq. (29) enforces that the intrinsic parameters of both the template and the signal are the same at the start of the waveform $t = t_0$. This implies that the component masses $m_{1,2}$, or equivalently the mass ratio $q = m_1/m_2 \geq 1$ and the total mass $M = m_1 + m_2$, and the dimensionless spins $\chi_{1,2}$ of the signal and the template are identical at t_0 [137].

For the calculation of the unfaithfulness we consider a total-mass range of $20\ M_\odot \leq M \leq 200\ M_\odot$. We show in Fig. 3 the 22-mode unfaithfulness maximized over the total-mass range for the SEOBNRv4 and SEOBNRv4E models. We remind the reader that the SEOBNRv4 model was calibrated requiring an unfaithfulness for the 22-mode against the 141 NR waveforms of at most of 1%. It is interesting to note that the SEOBNRv4E eccentric model achieves a similar accuracy, with the median of the distribution slightly larger than the one of the SEOBNRv4 model. This is due to the fact that the SEOBNRv4E model contains eccentric corrections, which were not available when calibrating the SEOBNRv4 model to NR in the quasicircular limit.

The higher order multipoles included in SEOBNRv4EHM are the same as in SEOBNRv4HM (i.e., $(l, |m|) = \{(2,1),(3,3),(4,4),(5,5)\}$). When computing the unfaithfulness of the models with higher modes against NR, we include in the NR waveforms all the modes with $l \leq 5$ as done in Ref. [134]. To ease the visualization of the results, we compute the SNR-weighted mismatches defined in Eq. (26), and average over the signal inclination,

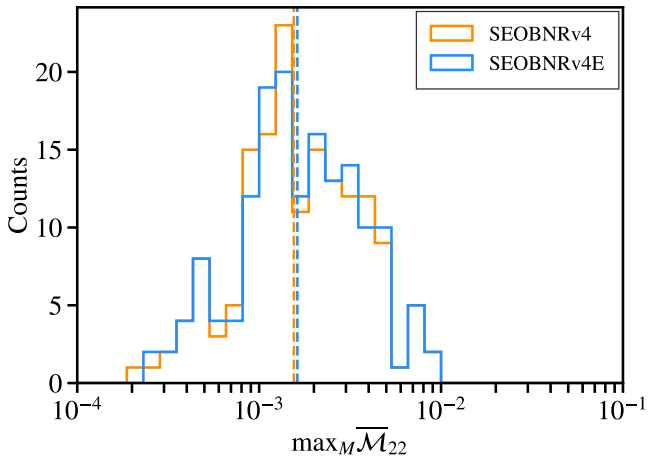

FIG. 3. Distribution of the maximum unfaithfulness of SEOBNRv4 (orange) [132] and the new SEOBNRv4E (blue) against the public 141 quasicircular NR simulations of Ref. [132]. The total mass range considered is $20\ M_\odot \leq M \leq 200\ M_\odot$. The calculations are done with the Advanced LIGO's zero-detuned high-power design sensitivity curve [158]. The vertical dashed orange (blue) lines correspond to the median values of the SEOBNRv4 (SEOBNRv4E) distributions.

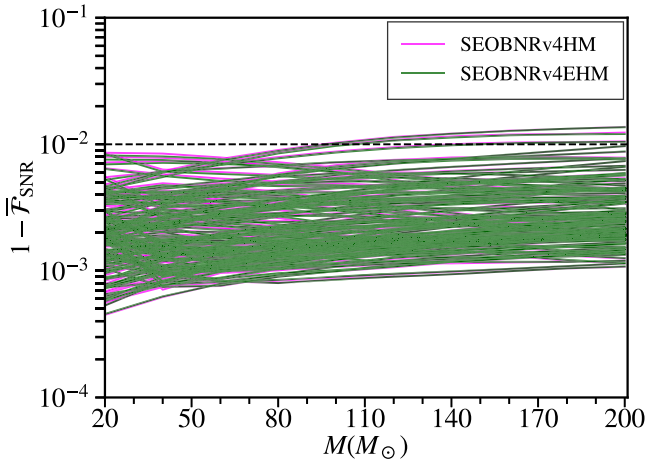

FIG. 4. SNR-weighted unfaithfulness, as defined in Eq. (28), as a function of the total mass, in the range $20\ M_\odot \leq M \leq 200\ M_\odot$, between the SEOBNRv4HM (pink) and SEOBNRv4EHM (green) models and the SXS quasicircular NR waveforms used in Ref. [134]. The calculations are done with the Advanced LIGO's zero-detuned high-power design-sensitivity curve [158], which is an estimate for the upcoming O4 run. The horizontal black dashed line indicates the 1% unfaithfulness value.

azimuthal and effective polarization angles. In practice, the average is performed over three different inclination angles of the signal $\iota_s = \{0, \pi/3, \pi/2\}$, and for each inclination angle we make a grid of 8×8 for $\kappa_s, \varphi_{0s} \in [0, 2\pi]$. In Fig. 4, we show the SNR-weighted mismatches for the SEOBNRv4HM and SEOBNRv4EHM models against the quasicircular NR waveforms at our disposal. Again, we note that the mismatches of the SEOBNRv4EHM model are very similar to the ones of the SEOBNRv4HM model. There are a few cases at high total masses for which both models have unfaithfulness above 1%, but not larger than 1.5%, as reported also in Ref. [134]. This indicates that the higher-order modes in the eccentric model have a comparable accuracy to the ones of the underlying quasicircular model in the zero eccentricity limit.

C. Comparison against eccentric numerical-relativity waveforms

The calculation of the unfaithfulness assumes that the intrinsic parameters of both template and signal are identical at the start of the evolution, that is we use the condition $\mathbf{\Theta}_s(t_s = t_{0_s}) = \mathbf{\Theta}_t(t_t = t_{0_t})$ in Eq. (24). In the eccentric case, this would imply that the mass ratio, q, total mass, M, dimensionless spins, $\chi_{1,2}$, eccentricity, e and relativistic anomaly, ζ, of both the signal and the template are the same at the start of the waveform. While the spins and mass parameters are uniquely fixed in the nonprecessing spinning case, the eccentricity and relativistic anomaly cannot be uniquely identified with respect to the NR waveforms. Consequently, when comparing a waveform

model against eccentric NR waveforms,[3] an optimization over the initial eccentricity and relativistic anomaly has to be performed to take into account the different definition of eccentricity between the model and the NR waveforms.

In the case of the SEOBNRv4EHM model, to reduce the dimensionality of the parameter space, we use the initial conditions for eccentric orbits starting at periastron ($\zeta = 0$), and we compute the eccentric EOB waveforms by specifying the initial eccentricity, e_0, and starting frequency, ω_0. Thus, when computing the faithfulness of the model against eccentric NR waveforms we have to maximize over e_0 and ω_0. Furthermore, here we compute the unfaithfulness using also another publicly available eccentric EOB model, TEOBResumSE[4] [121,123,124,127], for which we also specify initial conditions at periastron, and optimize over the initial eccentricity and starting frequency of the model. We note that although the TEOBResumSE can include higher-order modes, we use here only the $(2, |2|)$-modes, as we have found that in the presence of eccentricity some of the higher-order modes develop unphysical behaviors close to merger and ringdown. These features are likely due the treatment of the NQC corrections in the eccentric case, as already reported in Ref. [124].

First, we focus on the $(2, |2|)$-modes only waveforms. We define the eccentric faithfulness function as follows,

$$\mathcal{F}_{22}^{\rm ecc}(M_{\rm s}, \varphi_{0{\rm s}}) = \max_{t_{0_t}, \varphi_{0t}, e_0, \omega_0} \left[\frac{\langle h_s | h_t \rangle}{\sqrt{\langle h_s | h_s \rangle \langle h_t | h_t \rangle}} \bigg|_{\mathbf{\Theta}_{\rm s}(t_{\rm s}=t_{0_{\rm s}}) = \mathbf{\Theta}_t(t_t = t_{0_{\rm t}})} \right]. \quad (31)$$

For completeness, we introduce here also the unfaithfulness function as

$$\bar{\mathcal{M}}_{22}^{\rm ecc} = 1 - \bar{\mathcal{F}}_{22}^{\rm ecc}. \quad (32)$$

From Eq. (31) one observes that in the eccentric case two additional numerical optimizations have to be performed, as compared to the quasicircular case [see Eq. (29)]. The main difficulty of estimating such optimal values arises from the fact that the two additional optimizations cannot be easily performed with standard optimization algorithms, as the unfaithfulness has a highly oscillatory behavior as a function of these parameters. This can be observed in Fig. 5 where we show the unfaithfulness of the SEOBNRv4E waveform against the SXS:BBH:1355 waveform as function of the starting frequency. In Fig. 5, the mismatch is computed for a total mass of 20 $M_\odot$ and at fixed initial eccentricity $e_0 = 0.09$ for the SEOBNRv4E model. The high number of local maxima and minima in the unfaithfulness function makes standard optimization algorithms quite inefficient, and it increases substantially the computational cost of such procedure.

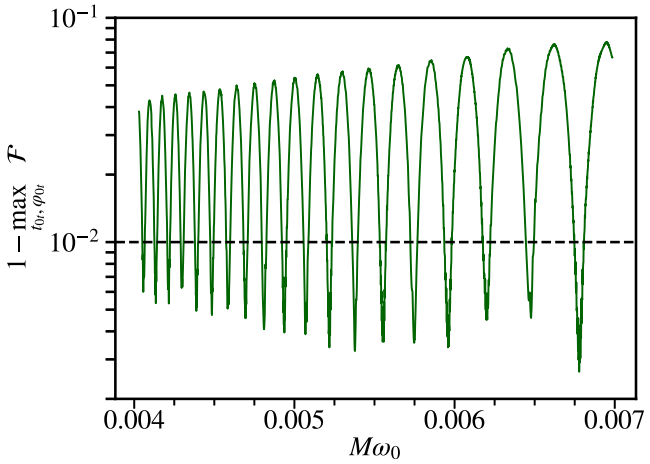

FIG. 5. Unfaithfulness of the SEOBNRv4E waveform model against the SXS:BBH:1355 waveform at a fixed initial eccentricity, $e_0 = 0.09$, as a function of the starting frequency of the model $M\omega_0$. The unfaithfulness is computed at a fixed total mass of 20 $M_\odot$, maximizing over the coalescence time, t_{0_t}, and azimuthal angle, φ_{0_t}, of the model.

In order to overcome this problem, different eccentric EOB models use different approaches to estimate the optimal values for e_0 and ω_0. In the case of the SEOBNREHM model [119,120,122] (not to be confused with our SEOBNRv4EHM model here), the starting frequency is set to the frequency when the eccentricity is estimated from the NR waveforms, and then the initial eccentricity is varied to get the best match against the NR waveforms. While for the TEOBResumSE model, the eccentricity and starting frequency are varied manually to get the lowest unfaithfulness against NR [123].

Here, we develop an automatic procedure to perform the two optimizations over e_0 and ω_0. The procedure is as follows:

(1) Fix the total mass to the lower bound of the total mass range used, that is 20 $M_\odot$. In this way, we ensure that more inspiral part of the NR waveform is in the frequency band of the mismatch calculation.
(2) Create a grid in eccentricity of N_e values around the value of the eccentricity as measured from the NR orbital frequency using Eq. (18), $e^{\rm NR}_{\omega_{\rm orb}}$, such that $e_0 \in [e^{\rm NR}_{\omega_{\rm orb}} - \delta e, e^{\rm NR}_{\omega_{\rm orb}} + \delta e]$. The value of δe determines the eccentricity interval. In the case $e^{\rm NR}_{\omega_{\rm orb}} - \delta e < 0$, we take the lower bound to be zero.
(3) For each value of the eccentricity, generate a grid of N_ω values of starting frequency. The upper bound is determined by the frequency at which the EOB

[3]Except in the case of the eccentric NR surrogate model [106], which is constructed with the same definitions of eccentricity and mean anomaly used to measure these parameters from NR waveforms.

[4]In this work, we use the eccentric branch of the public bitbucket repository https://bitbucket.org/eob_ihes/teobresums with the git hash 39e6d7723dacb23220ff5372e29756e5f94cb004, which is the latest at the time of this publication.

waveform equals the length l of the eccentric NR waveform, $\omega_0^{l_{\rm NR}=l_{\rm EOB}}$, while the lower bound is determined by a chosen $\delta\omega$. Thus, the frequency grid is $\omega_0 \in [\omega_0^{l_{\rm NR}=l_{\rm EOB}} - \delta\omega, \omega_0^{l_{\rm NR}=l_{\rm EOB}}]$.

(4) For each point in the grid, compute the unfaithfulness optimizing over the time shift and phase offset of the template as in Eq. (29).
(5) Store the values $(e_0^{\rm opt}, \omega_0^{\rm opt})$ which provide the lowest unfaithfulness.
(6) In order to reduce the computational cost, we use the optimal values, $(e_0^{\rm opt}, \omega_0^{\rm opt})$ at 20 $M_\odot$ for the whole mass range.

For the results in this paper we choose $N_e = 200$, $N_f = 500$, an eccentricity interval, $\delta e = 0.1$, and a starting frequency interval of $\delta f = 10$ Hz at 20 $M_\odot$, which translates into $\delta\omega = 0.006$.

The above optimization procedure is tested by computing the unfaithfulness against the eccentric NR waveforms publicly available in the SXS catalog [107,141]. In Table I we summarize the main properties of the NR simulations used in this work, the optimal values of initial eccentricity and starting frequency of the SEOBNRv4E and TEOBResumSE models, and the maximum value over total mass range of the unfaithfulness of the models against the NR simulations. We note that there is a particular simulation SXS:BBH:1169 for which the optimization procedure leads to zero initial eccentricity for TEOBResumSE. This is a NR simulation with very low eccentricity for which the quasicircular waveform has already a very low mismatch of 0.78%. The reported value of the unfaithfulness of TEOBResumSE for this case in Table I is slightly lower than that reported in Refs. [123,124]. We have checked modifications of the grid parameters in the eccentricity and starting frequency grids for the optimization procedure, particularly increasing the resolution up to $N_e = 300$ and $N_f = 1000$, but this optimal eccentricity

TABLE I. Summary of the eccentric NR simulations used in this work [107,141]. Each simulation is specified by the mass ratio $q = m_1/m_2 \geq 1$, z-component of the dimensionless spin vectors, $\chi_{1,2}$, the NR orbital frequency $\omega_{\rm orb,p}$, the eccentricity measured from the NR orbital frequency $e_{\omega_{\rm orb,p}}$, the (2, 2)-mode frequency $\omega_{22,p}$, and the eccentricity measured from the (2, 2)-mode frequency $e_{\omega_{22,p}}$, all evaluated at first periastron passage. For each simulation we report also the optimal values of the starting orbital frequency and eccentricity at periastron, (ω_p, e_{ω_p}), for the SEOBNRv4E and TEOBResumSE waveform models, as well as the maximum mismatch over the total mass range using such optimal values against the NR waveforms.

	Numerical-relativity simulations							SEOBNRv4E			TEOBResumSE		
ID	q	χ_1	χ_2	$\omega_{\rm orb,p}$	$e_{\omega_{\rm orb,p}}$	$\omega_{22,\rm p}$	$e_{\omega_{22,\rm p}}$	ω_p	e_{ω_p}	$1-\bar{\mathcal{F}}_{\rm max}[\%]$	ω_p	e_{ω_p}	$1-\bar{\mathcal{F}}_{\rm max}[\%]$
SXS:BBH:0089	1	−0.5	0.0	0.0128	0.06	0.025	0.048	0.0123	0.064	0.15	0.0111	0.064	0.64
SXS:BBH:0321	1	0.33	−0.44	0.0204	0.06	0.04	0.05	0.0196	0.07	0.22	0.0176	0.067	0.67
SXS:BBH:0322	1	0.33	−0.44	0.0223	0.075	0.0434	0.061	0.0224	0.086	0.35	0.0198	0.085	0.63
SXS:BBH:0323	1	0.33	−0.44	0.0235	0.126	0.045	0.102	0.0226	0.143	0.24	0.022	0.143	0.72
SXS:BBH:0324	1	0.33	−0.44	0.0303	0.246	0.0554	0.172	0.0299	0.297	0.3	0.0287	0.286	0.8
SXS:BBH:1136	1	−0.75	−0.75	0.0244	0.09	0.0475	0.076	0.0231	0.113	0.31	0.0209	0.113	0.24
SXS:BBH:1149	3	0.7	0.6	0.0197	0.048	0.0385	0.037	0.0189	0.045	0.3	0.0164	0.046	0.27
SXS:BBH:1169	3	−0.7	−0.6	0.0156	0.045	0.0306	0.037	0.016	0.046	0.39	0.0115	0.0	0.79
SXS:BBH:1355	1	0.0	0.0	0.0216	0.073	0.0421	0.059	0.0208	0.086	0.23	0.0189	0.07	0.79
SXS:BBH:1356	1	0.0	0.0	0.0182	0.127	0.0347	0.1	0.0179	0.145	0.24	0.0172	0.145	0.66
SXS:BBH:1357	1	0.0	0.0	0.0238	0.139	0.0453	0.112	0.0231	0.162	0.24	0.0224	0.159	0.74
SXS:BBH:1358	1	0.0	0.0	0.0243	0.137	0.0464	0.111	0.0237	0.164	0.14	0.0226	0.148	0.74
SXS:BBH:1359	1	0.0	0.0	0.0247	0.136	0.0472	0.111	0.0238	0.158	0.17	0.0234	0.162	0.69
SXS:BBH:1360	1	0.0	0.0	0.0278	0.192	0.0522	0.156	0.0272	0.232	0.2	0.0259	0.218	0.78
SXS:BBH:1361	1	0.0	0.0	0.028	0.194	0.0528	0.162	0.0277	0.239	0.24	0.0262	0.221	0.7
SXS:BBH:1362	1	0.0	0.0	0.0319	0.255	0.0584	0.193	0.0313	0.308	0.4	0.0305	0.309	0.73
SXS:BBH:1363	1	0.0	0.0	0.0321	0.257	0.0596	0.221	0.0313	0.304	0.48	0.0305	0.307	0.74
SXS:BBH:1364	2	0.0	0.0	0.0215	0.059	0.0421	0.048	0.0203	0.059	0.49	0.0185	0.066	0.46
SXS:BBH:1365	2	0.0	0.0	0.0215	0.083	0.0418	0.067	0.021	0.101	0.25	0.0191	0.101	0.29
SXS:BBH:1366	2	0.0	0.0	0.0239	0.134	0.0456	0.111	0.0233	0.158	0.2	0.0226	0.152	0.29
SXS:BBH:1367	2	0.0	0.0	0.0251	0.125	0.048	0.102	0.028	0.126	0.5	0.0264	0.113	0.92
SXS:BBH:1368	2	0.0	0.0	0.0244	0.132	0.0466	0.107	0.0236	0.151	0.32	0.0233	0.157	0.33
SXS:BBH:1369	2	0.0	0.0	0.0309	0.257	0.0573	0.191	0.0305	0.304	0.35	0.0299	0.308	0.39
SXS:BBH:1370	2	0.0	0.0	0.0315	0.25	0.0585	0.144	0.0312	0.301	0.31	0.0301	0.296	0.45
SXS:BBH:1371	3	0.0	0.0	0.0213	0.078	0.0414	0.063	0.0191	0.101	0.16	0.0191	0.093	0.15
SXS:BBH:1372	3	0.0	0.0	0.0237	0.13	0.0454	0.107	0.0233	0.153	0.19	0.0228	0.153	0.26
SXS:BBH:1373	3	0.0	0.0	0.0239	0.129	0.0458	0.104	0.0234	0.151	0.29	0.0229	0.149	0.21
SXS:BBH:1374	3	0.0	0.0	0.0306	0.248	0.0562	0.206	0.0304	0.294	0.33	0.0296	0.293	0.31

value of zero still remains unchanged. While it is possible that further increasing the resolution could lead to a slightly lower unfaithfulness, it also significantly increases the computational cost and therefore we opt to use the already calculated value. We also note that for this particular case (which has low eccentricity and high spins) the optimization procedure may be affected by the slight discontinuity of the TEOBResumSE model for small eccentricities as already noted in Ref. [72].

The unfaithfulness of the SEOBNRv4E and TEOBResumSE models against the dataset of eccentric NR waveforms described in Table I are shown in the upper panel of Fig. 6. We note that the unfaithfulness curves are always below 1% for the whole dataset and total mass ranges. These results also indicate that the approximation in step 6) of using the same optimal values for $(e_0^{\rm opt}, \omega_0^{\rm opt})$ for the whole total mass range is reasonable, as the unfaithfulness does not significantly increase with the total mass range. The bulk of the unfaithfulness curves for the SEOBNRv4E model is below the ones of the TEOBResumSE model for the NR dataset considered here. We note that the values of the unfaithfulness for the TEOBResumSE model reported here are similar to the ones in Ref. [123]. However, in a recent publication [124,127], lower unfaithfulnesses are reported for the TEOBResumSE model, driven by recalibrating it to quasicircular NR waveforms, and by better computing the Fourier transform of the time-domain waveforms, as remarked in Ref. [124,127]. (This improved model is not public.) As a consequence of those improvements, the main bulk of the unfaithfulness curves is closer to 10^{-3} values, and thus, at a similar level as the SEOBNRv4E model in Fig. 6. We remark that in order to better assess the accuracy of both models, comparisons against larger datasets of eccentric NR simulations are required. Eventually, Bayesian inference analyses will be needed to assess biases in the recovered parameters.

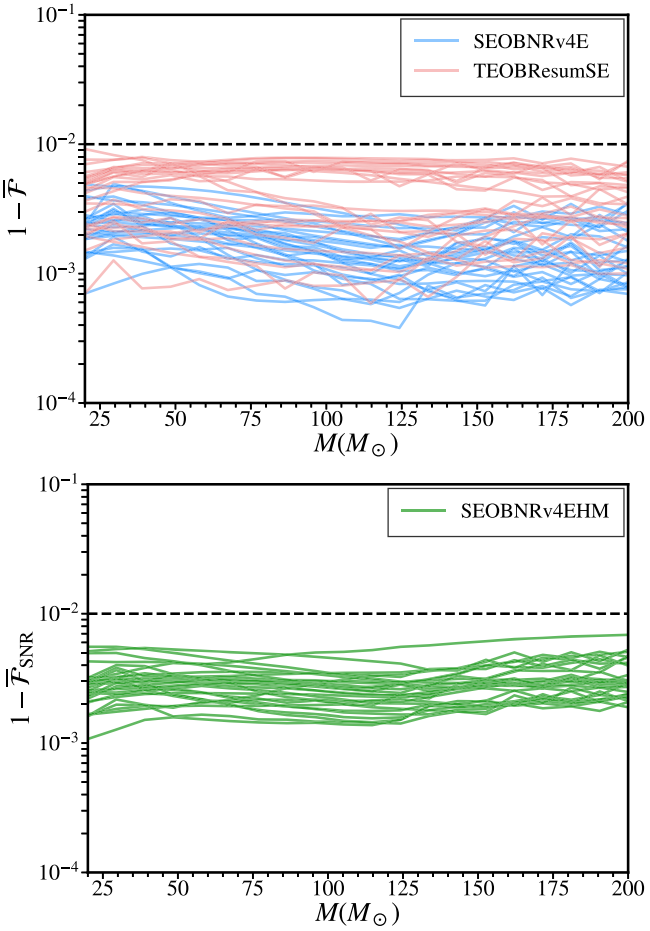

FIG. 6. Upper panel: unfaithfulness of the SEOBNRv4E and TEOBResumSE models against the 28 eccentric public SXS simulations listed in Table I. The calculations are performed optimizing over the initial eccentricity and starting frequency at periastron. Lower panel: unfaithfulness of SEOBNRv4EHM model against the same NR waveforms as in the upper panel, but including all modes with $l \leq 5$ in the NR waveforms. The calculations are performed using the optimal values of eccentricity and starting frequency obtained from the unfaithfulness computed with SEOBNRv4E. The horizontal dashed lines in both panels indicate the 1% value of unfaithfulness.

The calculation of the unfaithfulness including higher order modes requires three numerical optimizations (initial eccentricity, starting frequency and azimuthal angle of the template) and an analytical optimization over the effective polarization angle for each single point in the sky of the signal. Consequently, computing SNR-weighted unfaithfulness averaged over the sky-positions, orientations and inclinations of the signal becomes computationally prohibitive. In order to reduce the computational cost, we assume that the optimal values for the initial eccentricity and starting frequency of the SEOBNRv4EHM model are the same as the ones obtained for the SEOBNRv4E model, $(e_0^{\rm opt}, \omega_0^{\rm opt})$, and we compute the unfaithfulness as in the quasicircular case, numerically optimizing over the azimuthal angle of the template, and analytically over the effective polarization angle of the template.

We apply this approximation and compute the unfaithfulness between the SEOBNRv4EHM waveforms and the eccentric NR waveforms, which include all the modes with $l \leq 5$. We show the results in the lower panel of Fig. 6. We can observe that the curves of the SNR-weighted unfaithfulness for the multipolar model are always below 1%. This indicates that the approximation of using the optimal values of $(e_0^{\rm opt}, \omega_0^{\rm opt})$ obtained from the unfaithfulness of the SEOBNRv4E model is a good approximation. When comparing the unfaithfulness of the SEOBNRv4EHM model against the SEOB model developed in Ref. [122] (SEOBNREHM), we find that the unfaithfulness of SEOBNRv4EHM are always smaller than 1%, which is not the case for the SEOBNREHM model, which presents some cases with unfaithfulness as large as 2% [122]. We also note that the unfaithfulness for the SEOBNRv4EHM

model is overall larger than that for the SEOBNRv4E model, this may indicate that the higher-order modes in the multipolar model are not as accurately modeled as the dominant (2, 2) mode. However, we remark that the procedure to compute the unfaithfulness for the model with higher-order modes is suboptimal as the values of $(e_0^{\rm opt}, \omega_0^{\rm opt})$ are obtained from the SEOBNRv4E model, thus the unfaithfulness results for SEOBNRv4EHM are a conservative estimate. Furthermore, some higher-order modes in the dataset of the eccentric NR waveforms are affected by numerical noise, which may also affect the unfaithfulness values. This can also be seen in Fig. 7 where the different multipoles of the SEOBNRv4EHM waveform model for the optimal values of $(e_0^{\rm opt}, \omega_0^{\rm opt})$, and of the NR waveform SXS:BBH:1364 are shown. We note that the higher-order modes of the model have very good agreement with respect to NR, and that the early inspiral of the NR (5, 5)-mode is dominated by numerical noise. Thus, larger datasets of more accurate eccentric NR waveforms are required in order to better assess and improve the accuracy of multipolar eccentric EOB waveform models.

D. Robustness of the model across parameter space

Having assessed the accuracy of the model against the NR waveforms at our disposal, we now explore the region of validity of the SEOBNRv4EHM waveform model and identify the regions of parameter space where the model can be robustly generated.

One important property of a waveform model is its smoothness under small perturbations of the intrinsic parameters. In order to test this property, we compute the unfaithfulness between the SEOBNRv4E waveforms

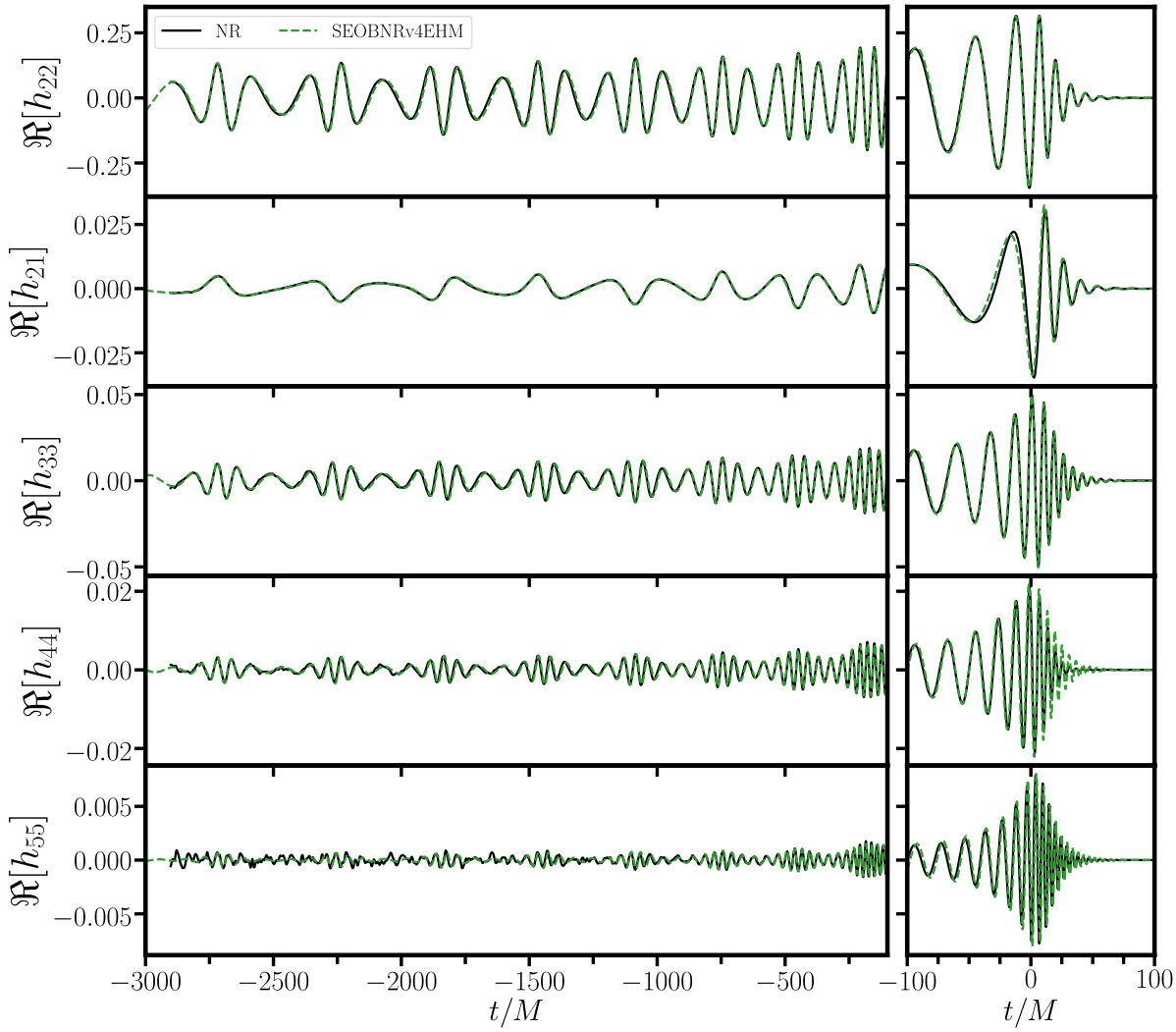

FIG. 7. From top to bottom, real part of the (2, 2),(2, 1), (3, 3), (4, 4) and (5, 5) modes in the time domain. The black curve corresponds to the NR simulation SXS:BBH:1369, which has mass ratio $q = 2$, zero spins, and eccentricity $e_{\omega_{\rm orb,p}} = 0.257$, while the green curve corresponds to the SEOBNRv4EHM model for the values of eccentricity and starting frequency that lead to the lowest unfaithfulness for the (2, 2) mode.

perturbing the eccentricity parameter by $\delta e = 10^{-7}$. We perform this test using the `pycbc_faithsim` function in the `PyCBC` software [163] and employ for 10^6 waveforms randomly distributed in the following parameter space: $\chi_{1,2} \in [-0.99, 0.99]$, $q \in [1, 20]$, $M \in [10, 100] M_\odot$, $e_0 \in [0, 0.3]$. We choose 19 Hz for the starting frequency of the waveforms, and 20 Hz for the overlap calculations. We find that only a few cases have unfaithfulness above 10^{-8}, with the maximum mismatch being 0.3% and the median mismatch being 0, indicating that the waveform model behaves smoothly under changes of the eccentricity parameter.

As an example, we show in Fig. 8 the amplitude and frequency of the multipoles in the `SEOBNRv4EHM` model (i.e., $(l, m) = \{(2, 2), (2, 1), (3, 3), (4, 4), (5, 5)\}$ modes), as function of time and aligned at the merger time, for different values of the mass ratio, for a configuration with initial eccentricity $e_0 = 0.25$, spins $(\chi_1, \chi_2) = (0.5, -0.75)$, starting frequency 20 Hz and with total mass 60 $M_\odot$. As can be seen, the modes of the `SEOBNRv4EHM` model have a smooth behavior in amplitude and frequency under variation of the mass ratio $q = 1 - 20$. We note that, during the inspiral, in the equal-mass case, the amplitude of the odd-m modes (except the (2, 1) mode) is very small compared to the unequal-mass configurations. The same behavior is present in the amplitudes of the quasicircular orbit `SEOBNRv4HM` model. As discussed in Ref. [134] (see Fig. 2 and text around), this is due to the fact that this binary configuration has a relatively large asymmetric-spin parameter $\chi_A = (\chi_1 - \chi_2)/2 = 0.5$, for which, in the equal-mass (or nearly equal-mass) case the odd-m modes (except the (2, 1)-mode) have very small amplitude during the inspiral, as predicted by PN theory.

We find that the orbit averaging procedure that we apply to the NQC function works quite well from large negative spins to mild positive spins, but binary's configurations with large-positive spins and small initial separation (or large dimensionless orbital frequency) can challenge this procedure due to the last periastron passage occurring very close to merger (see the Appendix B). This can cause oscillations in the dynamical quantities in the late inspiral. In order to test the smoothness of the waveform model in the large-spin region, we compute the unfaithfulness between two waveforms varying the spins in the region $\chi_{1,2} \in [0.8, 0.99]$ for 100 mass ratios $q \in [1, 50]$. For each

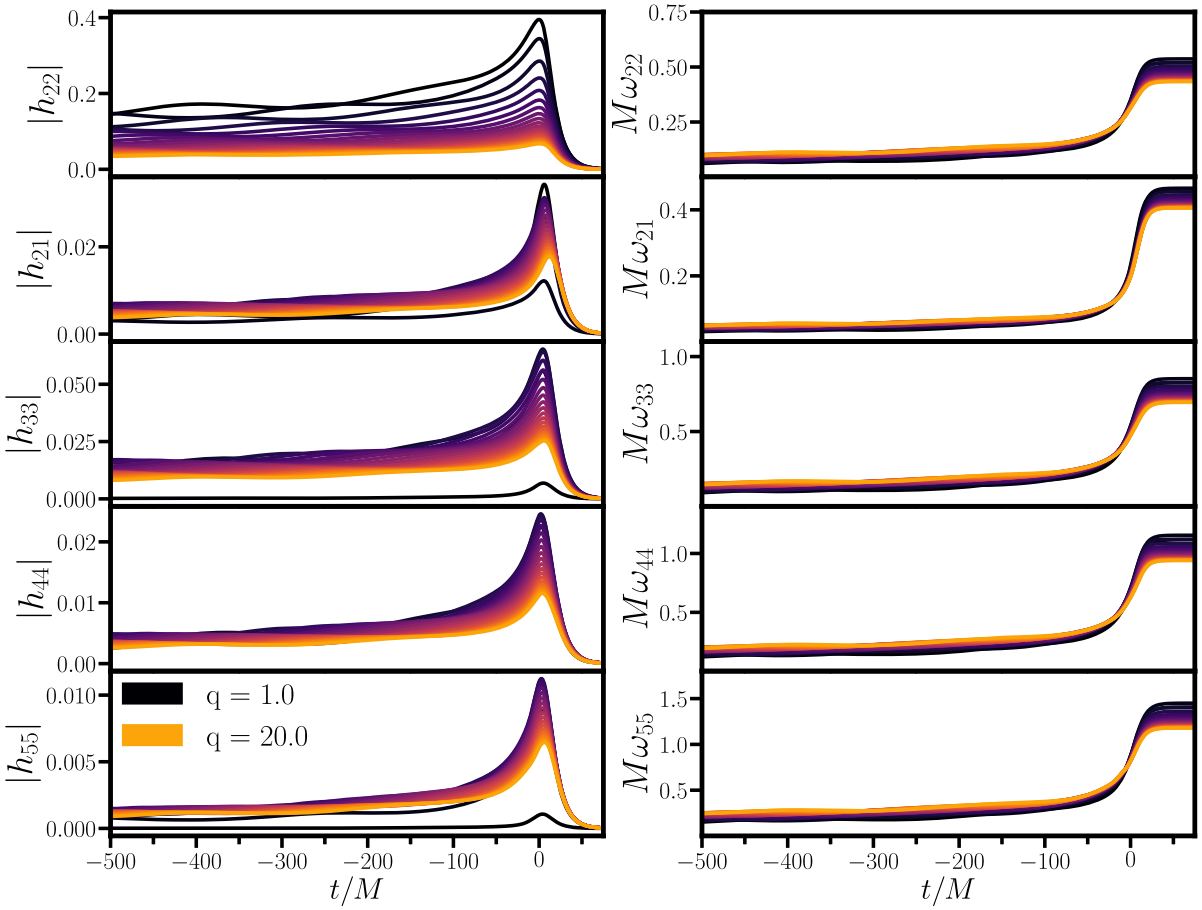

FIG. 8. From top to bottom amplitudes (left panels) and frequencies (right panels) of the (2, 2), (2, 1), (3, 3), (4, 4) and (5, 5) modes of `SEOBNRv4EHM` versus time, aligned at merger, for a configuration with initial eccentricity $e_0 = 0.25$, spins $(\chi_1, \chi_2) = (0.5, -0.75)$, starting frequency 20 Hz and total mass 60 $M_\odot$, for a mass ratio range $q \in [1, 20]$.

mass ratio, we compute the unfaithfulness between a waveform with $\chi_1 = \chi_2 = 0.8$, initial eccentricity 0.3 at starting frequency of 20 Hz and total mass 100 $M_\odot$ and waveforms with the same parameters but varying both $\chi_{1,2} \in [0.8, 0.99]$. This choice of total mass, starting frequency and eccentricity implies smaller initial separations of $r/M \sim 11$, and thus corresponds to a challenging case for the quasicircular assumption of the merger-ringdown signal. The results from such a test show an oscillatory unfaithfulness surface across parameter space without sharp features. We also observe that for $\chi_{1,2} \gtrsim 0.9 - 0.95$ the frequency of the (2, 2)-mode can have small spurious oscillations, thus, the model should be used with caution in this region of parameter space. Nevertheless, the model does not show prominent features in the waveform, and therefore, we recommend that it is used up to spins 0.99, eccentricity 0.3 and initial frequency up to 20 Hz. We plan to improve the model in the transition from plunge to merger for large spins, as soon as we will have access to NR eccentric waveforms with large spins.

We note that whereas we have probed the validity of the model through comparisons to the public SXS eccentric waveforms and internal consistency tests mostly for mass ratios $q \in [1, 20]$ and eccentricities $e \in [0, 0.3]$ at 20 Hz, we can also generate SEOBNRv4EHM waveforms at higher eccentricities and mass ratios, as illustrated in Fig. 9, where

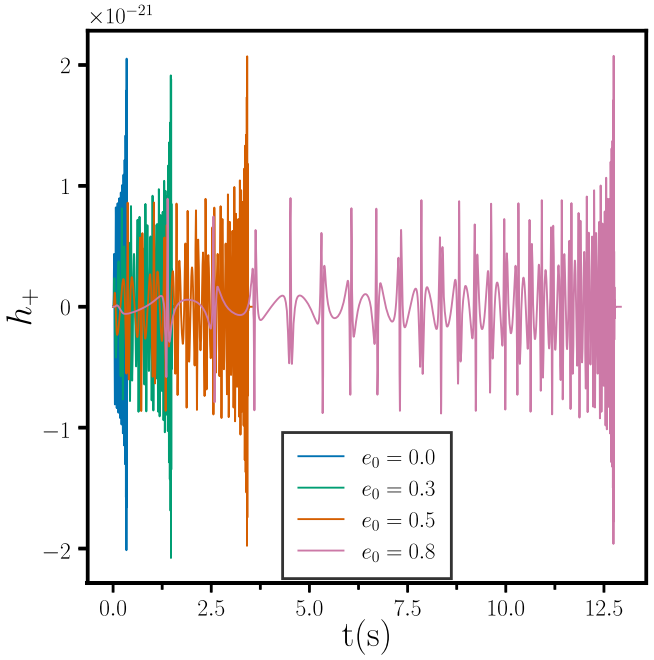

FIG. 9. Plus gravitational polarization versus time for a $q = 2$ nonspinning configuration computed with SEOBNRv4EHM for four different initial eccentricities $e_0 = [0, 0.3, 0.5, 0.8]$, and total mass $M = 100\ M_\odot$. All the configurations have a starting frequency of 20 Hz at periastron. We note that for $e_0 = 0.8$ the waveform reproduces the burstlike features produced at the periastron passages.

we show the plus polarization h_+ for a nonspinning BBH with mass-ratio 2 and different initial eccentricities $e_0 = [0, 0.3, 0.5, 0.8]$. These configurations are produced with a starting frequency of 20 Hz defined at periastron, so that, at that time, there are no frequencies in the inspiral higher than the starting frequency. In fact, we have checked that the model can be robustly generated at higher eccentricities by producing a large set of (10^6) waveforms randomly distributed in mass ratios $q \in [1, 50]$, spins $\chi_{1,2} \in [-0.99, 0.99]$, initial eccentricity $e_0 \in [0.3, 0.9]$ at a starting frequency of 20 Hz for binaries with total mass 80 $M_\odot$. In the generation of such dataset we do not find any waveform generation failure. However, lacking NR waveforms to compare against, we are not able to assess the accuracy and robustness of the model in this much larger region of the parameter space, so we recommend to use the model with caution for $e_0 > 0.3$.

Finally, we note that the region of parameter space with eccentricity up to 0.3 at 20 Hz is is of significant astrophysical interest. In fact, it is expected that most of the GW events detected with ground-based detectors, such as LIGO, Virgo and KAGRA, have small eccentricities $\lesssim 0.1$ [34,35,50,61], which are typically defined at 10 Hz.

The studies discussed in this section provide just a glance of all the internal checks performed to validate and implement the SEOBNRv4EHM waveform model in LALSuite [164], so that it is available to the large GW community as a tool to carry out inference studies of GW signals.

E. Unfaithfulness between eccentric and quasicircular waveforms

The impact of eccentricity in GW data analysis—for example Bayesian inference or GW searches—has been investigated in the literature [66–73,165–169], but it is mostly restricted to inspiral-only eccentric waveforms. Here, we start to extend these studies to IMR eccentric waveforms, exploring the region of parameter space in which we expect biases in estimating the source's properties if quasicircular-orbit waveforms were employed.

Using the SEOBNRv4EHM model, we compute the SNR-weighted unfaithfulness, averaged over the effective polarization angle and azimuthal angle of the signal, for an inclination angle of the source $\iota_s = \pi/3$ [Eq. (26)], against the quasicircular SEOBNRv4HM model in the following parameter space: $q \in [1, 20]$, $\chi_{1,2} \in [-0.95, 0.95]$, and $e_0 \in [0, 0.3]$. As an example, we consider a total mass of 70 $M_\odot$ and starting frequency of 20 Hz. We fix the initial conditions at periastron ($\zeta_0 = 0$) to reduce the dimensionality of the parameter space, and we set the starting frequency of the SEOBNRv4HM waveform, so that the length of the quasicircular waveform is the same as the eccentric one produced with SEOBNRv4EHM.

The unfaithfulness results are shown in Fig. 10. As expected, we observe that the unfaithfulness becomes increasingly large with eccentricity. We also appreciate a

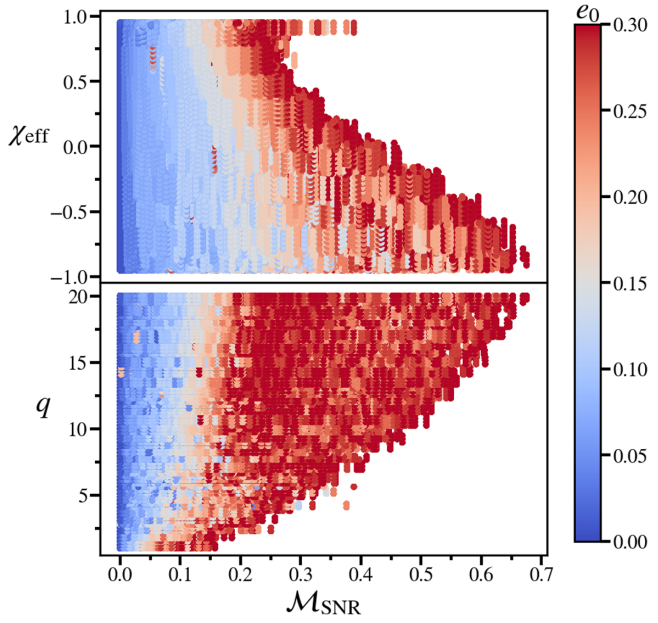

FIG. 10. SNR-weighted unfaithfulness, $\mathcal{M}_{\rm SNR} = 1 - \mathcal{F}_{\rm SNR}$, averaged over the effective polarization angle and azimuthal angle of the signal for an inclination angle of the signal $\iota_s = \pi/3$ as described in Eq. (26), between SEOBNRv4EHM and SEOBNRv4HM in the parameter space: $q \in [1, 20]$, $\chi_{1,2} \in [-0.95, 0.95]$, and $e_0 \in [0, 0.3]$. The total mass considered here is 70 $M_\odot$, and the starting frequency is 20 Hz. The calculations are done with the Advanced LIGO's zero-detuned high-power design sensitivity curve [158]. In the upper panel, we show the effective spin parameter, $\chi_{\rm eff}$, defined in Eq. (B3), as a function of SNR-weighted unfaithfulness. In the lower panel, we show the same quantity as in the upper one, but using mass ratio, q, in the y-axis. The color bar indicates the value of the initial eccentricity, e_0.

dependence of the results on the mass ratio and the effective-spin parameter. In the latter case, we observe that the unfaithfulness can be as large as ∼70% for large negative spins, while for positive spins the largest values occur at $\chi_{\rm eff} \sim 0.95$. The unfaithfulness also shows a dependence on the mass ratio, with values up to ∼70% for $q \sim 20$, while for comparable masses the unfaithfulness can be as large as 30%.

We note that large values of the unfaithfulness can imply large biases in source's parameters, if the quasicircular models were employed in inference studies against eccentric GW signals. Moreover, large unfaithfulness can also lead to a loss in SNR, which can make the GW modeled searches suboptimal [165,166]. The weighting of the unfaithfulness by the SNR (see Eq. (26), provides a conservative estimate of the upper limit of the fraction of detection volume lost. However, the unfaithfulness results presented here cannot be translated into an estimate of the sensitivity of a matched-filter search pipeline. This is because in a matched-filter search, the signal is compared against templates with different intrinsic parameters [162,170–172], which is not the case of our unfaithfulness study, where we have fixed the intrinsic parameters of the signal and the template to be the same. More comprehensive studies with GW signals that cover a large portion of the parameter space should be pursued in the future to assess the sensitivity of modeled searches to eccentric signals from BBHs with nonprecessing spins, and quantify the biases in the estimation of the parameters if quasicircular–orbit models were employed.

IV. CONCLUSIONS

Working within the EOB framework, we have developed the multipolar eccentric waveform model SEOBNRv4EHM for BBHs with nonprecessing spins and multipoles $(l, |m|) = \{(2,2), (2,1), (3,3), (4,4), (5,5)\}$. The eccentric waveform model is built upon the multipolar quasicircular SEOBNRv4HM model [132,134]. The inspiral waveform model SEOBNRv4EHM includes recently computed eccentric corrections up to the 2PN order [126], including the spin-orbit and spin-spin interactions, in the factorized GW modes. By contrast the merger and ringdown description of the SEOBNRv4EHM model is not modified with respect to the one in the quasicircular orbit case. Thus, we assume that the binary circularizes by the time it merges, and this is in agreement with NR simulations for mild eccentricities [107,173].

We have generalized the eccentric initial conditions introduced in Ref. [126] to include two eccentric parameters, the initial eccentricity e_0, and the initial relativistic anomaly ζ_0. Both parameters are specified at a certain starting frequency ω_0 along the elliptical orbit. We note that when the binary starts its evolution at periastron or apastron, one only needs to specify (e_0, ω_0), and this is the choice made in other eccentric EOB waveform models in the literature [121–124,127]. The relativistic anomaly is degenerate with variations of the initial orbital frequency ω_0 at fixed e_0. This fact is used to reduce the dimensionality of the parameter space when comparing EOB and NR waveforms in Sec. III C. For applications like Bayesian-inference studies, having generic initial conditions becomes essential as the parameters of a binary system are inferred at a fixed reference frequency [64]. Thus, for parameter-estimation studies, the starting frequency would be fixed, and the degeneracy between ω_0 and ζ_0 can no longer be used to accurately sample the eccentric parameter space.

We have also implemented the initial conditions for hyperbolic encounters and dynamical-capture systems, expressing them in terms of the initial angular momentum and energy at infinity [150]. As an example we have shown that the SEOBNRv4EHM model can qualitatively reproduce the behavior of dynamical captures. We leave to the future a quantitative and detailed study of the accuracy of the model for hyperbolic encounters, including comparisons with NR simulations of unbound systems.

Regarding the accuracy of our model, in the quasicircular limit we have found that the unfaithfulness between the

(2, 2)-mode only model, SEOBNRv4E, and the publicly available NR waveforms used to construct and validate the underlying quasicircular waveform model, SEOBNRv4 [132], is always smaller than 1%. When we include the higher order multipoles, $(l,|m|)=\{(2,1),(3,3),(4,4),(5,5)\}$, the unfaithfulness averaged over sky positions, orientations and inclinations between SEOBNRv4EHM and the same NR dataset used to validate SEOBNRv4HM, is overall below 1%, with few configurations above that threshold, but below 1.5%, as in the case of SEOBNRv4HM [134]. Thus, the multipolar eccentric model has an accuracy comparable to the underlying quasicircular model in the zero eccentricity limit.

To asses the accuracy of the model in the eccentric case, we have developed a maximization procedure of the unfaithfulness to estimate the optimal values of eccentricity and starting frequency. For the (2, 2)-mode waveforms, we have found that the unfaithfulness of the SEOBNRv4E model against the eccentric NR waveforms at our disposal, which have eccentricity $\lesssim 0.3$, is always smaller than 1%. We have also used another eccentric EOB waveform model TEOBResumSE to compute the unfaithfulness against eccentric NR waveforms, and we have found that the unfaithfulness is also always $< 1\%$. Overall we find that the unfaithfulness of SEOBNRv4E model is smaller than the public version of the TEOBResumSE model, at the time of this publication, for the NR dataset at our disposal. We note that in order to set more stringent constraints on the accuracy of both models, comparisons against larger datasets of eccentric NR simulations are required.

Considering that the accuracy of the SEOBNRv4EHM model against NR simulations can currently be investigated only up to eccentricity 0.3, we have assessed the smoothness and robustness of the SEOBNRv4EHM model in the parameter space $\chi_{1,2}\in[0.,0.99]$, $q\in[1,50]$ and $e=\in[0,0.3]$. We have found that some configurations when the spins are large and positive, notably in the range $\chi_{1,2}\in[0.95,0.99]$, lead to spurious oscillations in the amplitude and frequency close to merger. This is due to the suboptimal procedure used by the SEOBNRv4EHM model to transit from the late inspiral to the merger and ringdown. Furthermore, the SEOBNRv4EHM can be generated also for eccentricity larger than 0.3, however we caution its use for large eccentricities, especially beyond the inspiral phase, since the model has been built under the assumption that the binary circularizes. We emphasize that current GW detectors, such as LIGO, Virgo and KAGRA will be able to detect eccentric GW events with mild eccentricities [34,35]. Thus, having a waveform model that can grasp the main characteristic of eccentric signals up to eccentricity 0.3 is valuable—for example the SEOBNRv4EHM model could be employed to search for eccentric signals in the LIGO and Virgo data and to infer the properties of the eccentric sources.

We remark that in this first eccentric EOBNR model, we have only included the eccentric corrections up to 2PN order derived in Ref. [126] to the factorized GW modes, while we have kept the conservative and dissipative dynamics the same as in the quasicircular SEOBNRv4HM model. Preliminary comparisons with a larger set of NR simulations are indicating that better accuracy can be achieved when including the eccentric corrections [126] also in the RR forces. These improvements will be included in the next generation of the EOBNR waveform models currently under construction, that is the SEOBNRv5 model.

We leave to the near future the development of a reduced-order-model (ROM) [174,175] version of the SEOBNRv4EHM model, so that it can efficiently be used for inference studies on current GW catalogs and future observations with the LIGO, Virgo and KAGRA detectors. We also plan to extend the SEOBNRv4EHM model to precessing binaries, including the eccentric corrections to the waveform modes of the quasicircular spin-precessing SEOBNRv4PHM model [130,135,137].

ACKNOWLEDGMENTS

It is a pleasure to thank Jan Steinhoff and Justin Vines for helpful discussions. The computational work for this manuscript was carried out on the computer cluster Minerva at the Max Planck Institute for Gravitational Physics in Potsdam, and on the cluster CIT provided by the LIGO Laboratory and supported by the National Science Foundation Grants No. PHY0757058 and No. PHY-0823459. LIGO is funded by the U.S. National Science Foundation.

APPENDIX A: ECCENTRIC CORRECTIONS TO THE WAVEFORM MODES

In this Appendix, we list the eccentric corrections to the waveform modes obtained in Ref. [126]. These corrections are written in terms of the dynamical quantities r, p_r and $\dot{p}_r$. To ease the notation, we define

$$v_{\dot{\phi}}\equiv\frac{(\dot{p}_r r^2+1)^{1/6}}{\sqrt{r}}, \tag{A1}$$

which is $(\dot{\phi})^{1/3}$ at leading PN order for generic orbits, and it reduces to $v_\omega\equiv\omega^{1/3}$ in the circular-orbit limit. We also define the antisymmetric mass ratio $\delta\equiv(m_1-m_2)/M$ and the spin combinations

$$\chi_S=\frac{1}{2}(\chi_1+\chi_2),\qquad \chi_A=\frac{1}{2}(\chi_1-\chi_2). \tag{A2}$$

We expand the eccentric part of the leading-order tail term, $T^{\rm ecc}_{lm}$, in Eq. (6), in powers of the eccentricity up to $\mathcal{O}(e^6)$, and express it in terms of the dynamical quantities p_r and $\dot{p}_r$ as described in Ref. [126] using the Keplerian parametrization. For the $\{(2,2),(2,1),(3,3)\}$ modes, we obtain through 2PN order

$$T_{22}^{\rm ecc} = -\frac{\pi}{4c^3 r}\left[(4r^{3/2}\dot{p}_r + 6ip_r) + (2\sqrt{r}p_r^2 + ir^2 p_r\dot{p}_r) + \left(\frac{5}{4}r^{5/2}p_r^2\dot{p}_r + \frac{1}{12}r^{11/2}\dot{p}_r^3 - \frac{3}{4}ir^4 p_r\dot{p}_r^2 + \frac{5}{12}irp_r^3\right)\right.$$
$$+ \left(\frac{5}{4}r^{3/2}p_r^4 - r^{9/2}p_r^2\dot{p}_r^2 - \frac{1}{4}r^{15/2}\dot{p}_r^4 + \frac{1}{8}ir^6 p_r\dot{p}_r^3 - \frac{15}{8}ir^3 p_r^3\dot{p}_r\right)$$
$$+ \left(-\frac{115}{48}r^{7/2}p_r^4\dot{p}_r + \frac{101}{96}r^{13/2}p_r^2\dot{p}_r^3 + \frac{29}{120}r^{19/2}\dot{p}_r^5 - \frac{11}{96}ir^8 p_r\dot{p}_r^4 + \frac{53}{24}ir^5 p_r^3\dot{p}_r^2 - \frac{589}{480}ir^2 p_r^5\right)$$
$$+ \left(-\frac{329}{480}r^{5/2}p_r^6 + \frac{83}{32}r^{11/2}p_r^4\dot{p}_r^2 - \frac{257}{192}r^{17/2}p_r^2\dot{p}_r^4 - \frac{7}{36}r^{23/2}\dot{p}_r^6 + \frac{223}{960}ir^{10}p_r\dot{p}_r^5 - \frac{181}{72}ir^7 p_r^3\dot{p}_r^3 + \frac{111}{64}ir^4 p_r^5\dot{p}_r\right)$$
$$\left. + \mathcal{O}(p_r, \dot{p}_r)^8\right], \tag{A3}$$

$$T_{21}^{\rm ecc} = -\frac{\pi}{4c^4 r}\left[8ip_r + (-r^{7/2}\dot{p}_r^2 - 2ir^2 p_r\dot{p}_r + \sqrt{r}p_r^2) + \left(\frac{3}{2}r^{5/2}p_r^2\dot{p}_r + \frac{5}{6}r^{11/2}\dot{p}_r^3 + \frac{2}{3}irp_r^3\right)\right.$$
$$+ \left(\frac{7}{16}r^{3/2}p_r^4 - \frac{9}{4}r^{9/2}p_r^2\dot{p}_r^2 - \frac{7}{16}r^{15/2}\dot{p}_r^4 + \frac{5}{4}ir^6 p_r\dot{p}_r^3 - \frac{5}{4}ir^3 p_r^3\dot{p}_r\right)$$
$$+ \left(-\frac{79}{96}r^{7/2}p_r^4\dot{p}_r + 2r^{13/2}p_r^2\dot{p}_r^3 + \frac{33}{160}r^{19/2}\dot{p}_r^5 - \frac{11}{8}ir^8 p_r\dot{p}_r^4 + \frac{19}{12}ir^5 p_r^3\dot{p}_r^2 - \frac{19}{120}ir^2 p_r^5\right)$$
$$+ \left(-\frac{59}{320}r^{5/2}p_r^6 + \frac{145}{384}r^{11/2}p_r^4\dot{p}_r^2 - \frac{487}{384}r^{17/2}p_r^2\dot{p}_r^4 - \frac{161r^{23/2}\dot{p}_r^6}{1440} + \frac{511}{480}ir^{10}p_r\dot{p}_r^5 - \frac{115}{144}ir^7 p_r^3\dot{p}_r^3 + \frac{61}{160}ir^4 p_r^5\dot{p}_r\right)$$
$$\left. + \mathcal{O}(p_r, \dot{p}_r)^8\right], \tag{A4}$$

$$T_{33}^{\rm ecc} = -\frac{\pi}{81c^4 r}\left[(90r^{3/2}\dot{p}_r + 180ip_r) + (-11r^{7/2}\dot{p}_r^2 + 22ir^2 p_r\dot{p}_r + 56\sqrt{r}p_r^2)\right.$$
$$+ \left(2r^{5/2}p_r^2\dot{p}_r + \frac{331}{36}r^{11/2}\dot{p}_r^3 - \frac{8}{3}ir^4 p_r\dot{p}_r^2 + \frac{34}{9}irp_r^3\right)$$
$$+ \left(\frac{26161r^{3/2}p_r^4}{5184} + \frac{10895}{864}r^{9/2}p_r^2\dot{p}_r^2 - \frac{33191r^{15/2}\dot{p}_r^4}{5184} - \frac{2383ir^6 p_r\dot{p}_r^3}{1296} + \frac{14671ir^3 p_r^3\dot{p}_r}{1296}\right)$$
$$+ \left(\frac{3165361r^{7/2}p_r^4\dot{p}_r}{93312} - \frac{1286269r^{13/2}p_r^2\dot{p}_r^3}{46656} + \frac{2170663r^{19/2}\dot{p}_r^5}{466560} + \frac{17347ir^8 p_r\dot{p}_r^4}{2916} - \frac{252673ir^5 p_r^3\dot{p}_r^2}{5832} + \frac{590461ir^2 p_r^5}{58320}\right)$$
$$+ \left(\frac{269913797r^{5/2}p_r^6}{16796160} - \frac{1192721r^{11/2}p_r^4\dot{p}_r^2}{15552} + \frac{49153087r^{17/2}p_r^2\dot{p}_r^4}{1119744} - \frac{6543119r^{23/2}\dot{p}_r^6}{1679616} - \frac{10372969ir^{10}p_r\dot{p}_r^5}{933120}\right.$$
$$\left.\left. + \frac{63206059ir^7 p_r^3\dot{p}_r^3}{839808} - \frac{27211231ir^4 p_r^5\dot{p}_r}{559872}\right) + \mathcal{O}(p_r, \dot{p}_r)^8\right]. \tag{A5}$$

For the eccentric term $f_{lm}^{\rm ecc}$ in Eq. (6), and the modes $\{(2,2),(2,1),(3,3),(4,4),(5,5)\}$, we obtain

$$
\begin{aligned}
f_{22}^{\rm ecc} =& \frac{1-rp_r^2+r^3v_\phi^6-2rv_\phi^2}{2rv_\phi^2}+irv_\phi p_r+\frac{1}{84c^2r^5v_\phi^8}\{-14(\nu+1)+ir^2v_\phi^3p_r[14(\nu+1)+r^3v_\phi^6(-101\nu+(41\nu-37)r^3v_\phi^6-209)]\\
&+r^2p_r^4[(29-10\nu)r^3v_\phi^6-7(\nu-3)]+r^3v_\phi^6[63\nu+r^2v_\phi^4(-110\nu+(31\nu-8)r^4v_\phi^8+(30\nu-59)rv_\phi^2+172)-91]\\
&+p_r^2r[21\nu+3r^3v_\phi^6(3\nu+7(\nu+1)r^3v_\phi^6+62)-7]+ir^3v_\phi^3p_r^3[(41\nu-37)r^3v_\phi^6-7(\nu-3)]\}\\
&+\frac{1}{6048c^4r^9v_\phi^{14}}\{3i(103\nu^2-700\nu+127)r^{14}v_\phi^{27}p_r+6r^{12}v_\phi^{24}[318-4\nu(96\nu+265)+(40\nu^2+20\nu-71)rp_r^2]\\
&+6ir^{11}v_\phi^{21}p_r[80+1531\nu-640\nu^2+(349-143\nu^2-724\nu)rp_r^2]+24(55\nu-86)r^8v_\phi^{16}[1-\nu+(\nu+1)rp_r^2]\\
&+6r^9v_\phi^{18}[-616+955\nu-409\nu^2+(17\nu^2+193\nu-340)r^2p_r^4-(1181\nu^2+1277\nu+279)rp_r^2]\\
&-105ir^2v_\phi^3p_r[(\nu-3)rp_r^2-2(\nu+1)]^2+24(55\nu-86)r^5v_\phi^{10}[(\nu-3)rp_r^2-2(\nu+1)]\\
&+ir^8v_\phi^{15}p_r[13\nu(3598-517\nu)-3(389\nu^2+748\nu-571)r^2p_r^4+12(281\nu^2-349\nu+803)rp_r^2-9221]\\
&+6ir^5v_\phi^9p_r[50\nu^2-872\nu+(22\nu^2+55\nu-216)r^2p_r^4-(69\nu^2+674\nu+953)rp_r^2-166]\\
&+6r^3v_\phi^6[28(17\nu-16\nu^2+6)+(43\nu^2+13\nu-279)r^3p_r^6-(243\nu^2+325\nu+1253)r^2p_r^4+2(269\nu^2-446\nu+237)rp_r^2]\\
&+6r^6v_\phi^{12}[2\nu(733\nu-620)+(80\nu^2+130\nu-277)r^3p_r^6+(-294\nu^2+380\nu-1963)r^2p_r^4-2(205\nu^2+2604\nu+93)rp_r^2+26]\\
&-168(rp_r^2-1)[(\nu-3)rp_r^2-2(\nu+1)]^2+6(103\nu^2-43\nu-8)r^{15}v_\phi^{30}+24(\nu+1)(55\nu-86)r^{11}v_\phi^{22}\}\\
&+\frac{1}{6c^3r^4v_\phi^5}\{\chi_S[2-\nu+i(5\nu-8)r^2v_\phi^3p_r+(\nu-2)rp_r^2+r^3v_\phi^6(9\nu-8(\nu-1)rv_\phi^2-10)]\\
&-2\delta\chi_A[-1+4ir^2v_\phi^3p_r+rp_r^2+r^3v_\phi^6(5-4rv_\phi^2)]\}\\
&+\frac{1}{6c^4r^6v_\phi^8}\{2\delta\chi_A\chi_S[i(2\nu-1)r^3v_\phi^3p_r^3+rp_r^2(\nu+5(2\nu-1)r^3v_\phi^6+1)+(2\nu-1)r^2p_r^4-3ip_r(2(2\nu-1)r^5v_\phi^9-\nu r^2v_\phi^3)\\
&-3(r^3v_\phi^6-1)((2\nu+1)r^3v_\phi^6-\nu)]+\chi_S^2[rp_r^2(-2\nu^2+2\nu-5(1-2\nu)^2r^3v_\phi^6+1)-i(1-2\nu)^2r^3v_\phi^3p_r^3-(1-2\nu)^2r^2p_r^4\\
&+6ip_r((1-2\nu)^2r^5v_\phi^9-(\nu-1)\nu r^2v_\phi^3)+3(r^3v_\phi^6-1)((4\nu^2-4\nu-1)r^3v_\phi^6-2(\nu-1)\nu)]\\
&+\chi_A^2(4\nu-1)r[-6ir^4v_\phi^9p_r+p_r^2(5r^3v_\phi^6-1)+ir^2v_\phi^3p_r^3+rp_r^4+3r^2v_\phi^6(r^3v_\phi^6-1)]\}+\mathcal{O}\left(\frac{1}{c^5}\right),
\end{aligned}
\tag{A6}
$$

$$
\begin{aligned}
f_{21}^{\rm ecc} =& \frac{1-r^2v_\phi^4}{r^2v_\phi^4}\\
&-\frac{1}{42c^2r^6v_\phi^{10}}\{28(\nu+1)+3i(12\nu-83)r^5v_\phi^9p_r+r^3v_\phi^6(82-52\nu+(19\nu+106)rp_r^2)-14(\nu-3)rp_r^2+2(12\nu-55)r^6v_\phi^{12}\}\\
&+\frac{1}{4c\delta r^4v_\phi^7}[\chi_A(6r^4v_\phi^8-6)+6\delta(r^4v_\phi^8-1)\chi_S]+\frac{1}{336c^3\delta r^8v_\phi^{13}}\{\chi_A[588(\nu+1)+24i(104\nu-147)r^5v_\phi^9p_r+42(\nu-1)r^7v_\phi^{14}\\
&-6p_r^2(7(\nu+1)r^8v_\phi^{14}+7(\nu-3)r^5v_\phi^8-(141\nu+203)r^4v_\phi^6+49(\nu-3)r)-42(\nu+1)r^{10}v_\phi^{20}-4(131\nu+427)r^8v_\phi^{16}\\
&+30(121\nu-35)r^6v_\phi^{12}+84(\nu+1)r^4v_\phi^8+2(1085-1889\nu)r^3v_\phi^6]-2\delta\chi_S[-294(\nu+1)+36i(2\nu+49)r^5v_\phi^9p_r\\
&+3p_r^2(7(\nu+1)r^8v_\phi^{14}+7(\nu-3)r^5v_\phi^8-(69\nu+203)r^4v_\phi^6+49(\nu-3)r)+21(\nu+1)r^{10}v_\phi^{20}+2(79\nu+427)r^8v_\phi^{16}\\
&-21(\nu-1)r^7v_\phi^{14}+15(35-33\nu)r^6v_\phi^{12}-42(\nu+1)r^4v_\phi^8+(673\nu-1085)r^3v_\phi^6]\}+\mathcal{O}\left(\frac{1}{c^4}\right),
\end{aligned}
\tag{A7}
$$

$$
\begin{aligned}
f_{33}^{\mathrm{ecc}} = {} & \frac{2}{9rv_{\dot\phi}^3}[3ir^3v_{\dot\phi}^6p_r - 3r^2v_{\dot\phi}^3p_r^2 - irp_r^3 + 2ip_r + r^4v_{\dot\phi}^9 - rv_{\dot\phi}^3] \\
& + \frac{1}{162c^2r^5v_{\dot\phi}^9}\{-36(\nu-2)r^6v_{\dot\phi}^9p_r^4 + 6r^5v_{\dot\phi}^9p_r^2[18\nu-(\nu-11)r^3v_{\dot\phi}^6+57] \\
& + 6irp_r^3[6(\nu-1)+r^3v_{\dot\phi}^6(-4\nu+2(5\nu-1)r^3v_{\dot\phi}^6+35)] \\
& + 3r^4v_{\dot\phi}^9[56\nu + r^3v_{\dot\phi}^6(42\nu+2(5\nu-1)r^3v_{\dot\phi}^6-39)+27(7-4\nu)rv_{\dot\phi}^2-148] \\
& + ip_r[r^3v_{\dot\phi}^6(100\nu+9r^3v_{\dot\phi}^6(-23\nu+(7\nu-5)r^3v_{\dot\phi}^6-29)-218)-36(\nu+1)] - 3ir^2p_r^5[3(\nu-3)+(\nu-11)r^3v_{\dot\phi}^6]\} \\
& \times \frac{1}{18c^3\delta r^4v_{\dot\phi}^6}\{\chi_A[2ip_r(-16\nu+(101\nu-24)r^3v_{\dot\phi}^6+4)+2(6-25\nu)r^2v_{\dot\phi}^3p_r^2 \\
& + 4i(4\nu-1)rp_r^3 - 4(5\nu-1)rv_{\dot\phi}^3(r^3v_{\dot\phi}^6-1)] \\
& + 2\delta\chi_S[ip_r(-2\nu+(17\nu-24)r^3v_{\dot\phi}^6+4)+2(3-2\nu)r^2v_{\dot\phi}^3p_r^2 + i(\nu-2)rp_r^3 - (3\nu-2)rv_{\dot\phi}^3(r^3v_{\dot\phi}^6-1)]\} \\
& + \mathcal{O}\left(\frac{1}{c^4}\right),
\end{aligned} \tag{A8}
$$

$$
\begin{aligned}
f_{44}^{\mathrm{ecc}} = {} & \frac{1}{64r^2v_{\dot\phi}^4}\{7 + r[24ir^4v_{\dot\phi}^9p_r + 3r^2v_{\dot\phi}^6(17-12rp_r^2) - 6irv_{\dot\phi}^3p_r(4rp_r^2-9) + 6p_r^2(rp_r^2-3) + 6r^5v_{\dot\phi}^{12} - 64rv_{\dot\phi}^4]\} \\
& + \frac{1}{42240(3\nu-1)c^2r^6v_{\dot\phi}^{10}}\{-3r^9v_{\dot\phi}^{18}[60\nu(889-636\nu)+20(\nu(321\nu-926)+238)rp_r^2-10481] \\
& + 120i(267\nu^2-278\nu+49)r^{11}v_{\dot\phi}^{21}p_r + 6ir^8v_{\dot\phi}^{15}p_r[8033-5\nu(4551\nu+3622)+1320(\nu+1)(3\nu-1)rp_r^2] \\
& + r^6v_{\dot\phi}^{12}[-780\nu(234\nu-289)-60(519\nu^2-794\nu+172)r^2p_r^4+6(10\nu(2265\nu+1882)-9847)rp_r^2-46063] \\
& - 6ir^5v_{\dot\phi}^9p_r[5\nu(12748-2727\nu)+20(69\nu^2-410\nu+115)r^2p_r^4+(10277-5\nu(525\nu+5294))rp_r^2-20789] \\
& + 20r^3v_{\dot\phi}^6[3315\nu^2-2644\nu-3(15\nu^2+238\nu-74)r^3p_r^6+3(339\nu^2-1274\nu+422)r^2p_r^4 \\
& - 2(1797\nu^2-4910\nu+1510)rp_r^2+553] \\
& - 330i(3\nu-1)r^2v_{\dot\phi}^3p_r(4rp_r^2-9)[(\nu-3)rp_r^2-2(\nu+1)] + 220(3\nu-1)[6r(rp_r^2-3)p_r^2+7][(\nu-3)rp_r^2-2(\nu+1)] \\
& + 60(183\nu^2-106\nu+8)r^{12}v_{\dot\phi}^{24}\} + \mathcal{O}\left(\frac{1}{c^3}\right),
\end{aligned} \tag{A9}
$$

$$
\begin{aligned}
f_{55}^{\mathrm{ecc}} = {} & \frac{1}{625r^2v_{\dot\phi}^5}\{120ir^6v_{\dot\phi}^{12}p_r + 3r^4v_{\dot\phi}^9(143-80rp_r^2) - 48ir^3v_{\dot\phi}^6p_r(5rp_r^2-13) + 4rv_{\dot\phi}^3(30r^2p_r^4-99rp_r^2+43) \\
& + 24r^7v_{\dot\phi}^{15} - 625r^2v_{\dot\phi}^5 + 2ip_r[12r(rp_r^2-4)p_r^2+41]\} + \mathcal{O}\left(\frac{1}{c}\right).
\end{aligned} \tag{A10}
$$

For binaries of equal masses ($\delta = 0, \nu = 1/4$), the leading-PN order of the odd-m modes is proportional to δ, which cancels with the denominator of χ_A/δ in the above expressions for the (2, 1) and (3, 3) modes, leading to

$$
\begin{aligned}
f_{21}^{\mathrm{ecc},\delta=0} = {} & \frac{3\chi_A}{2cv_{\dot\phi}^7}\left(v_{\dot\phi}^8 - \frac{1}{r^4}\right) + \frac{\chi_A}{224c^3r^8v_{\dot\phi}^{13}}[rp_r^2(35r^7v_{\dot\phi}^{14} - 77r^4v_{\dot\phi}^8 - 953r^3v_{\dot\phi}^6 - 539) \\
& + 1936ir^5v_{\dot\phi}^9p_r + 35r^{10}v_{\dot\phi}^{20} + 1226r^8v_{\dot\phi}^{16} + 21r^7v_{\dot\phi}^{14} + 95r^6v_{\dot\phi}^{12} - 70r^4v_{\dot\phi}^8 - 817r^3v_{\dot\phi}^6 - 490],
\end{aligned} \tag{A11}
$$

$$
f_{33}^{\mathrm{ecc},\delta=0} = \frac{\chi_A}{36c^3r^3v_{\dot\phi}^3}[2 - r(-5irv_{\dot\phi}^3p_r + p_r^2 + 2r^2v_{\dot\phi}^6)]. \tag{A12}
$$

Since the eccentric correction to the (5, 5)-mode does not depend on spin at this order, it goes to zero for equal masses.

APPENDIX B: IMPLEMENTATION OF THE ORBIT AVERAGING PROCEDURE

In this Appendix, we describe in detail the orbit averaging procedure that we have applied in Sec. II B to the instantaneous NQC functions of the waveform.

According to Eq. (9), to orbit average a dynamical quantity we need to define the times, t_i, which identify successive orbits in the evolution. In our implementation, we use the local maxima and employ a simple algorithm that compares each element of the time series with the two closest neighbors. However, these values may strongly depend on the specified time step, thus, in order to reduce such dependence we further compute the parabola passing through these three points $\{(t_{i-1}, X_{i-1}), (t_i, X_i), (t_{i+1}, X_{i+1})\}$, and obtain its maxima analytically,

$$
\begin{aligned}
f(t) &= at^2 + bt + c, \qquad t_{\max} = -b/2a, \\
\Delta &= (t_i - t_{i+1})(t_i - t_{i-1})(t_{i+1} - t_{i-1}) \\
a &= \frac{1}{\Delta}[X_{i-1}(t_i - t_{i+1}) + X_i(t_{i+1} - t_{i-1}) \\
&\quad + X_{i+1}(-t_i + t_{i-1}))], \\
b &= \frac{1}{\Delta}[X_{i-1}(-t_i^2 + t_{i+1}^2) + X_{i+1}(t_i^2 - t_{i-1}^2) \\
&\quad + X_i(-t_{i+1}^2 + t_{i-1}^2)], \\
c &= \frac{1}{\Delta}[(X_{i-1}(t_i - t_{i+1})t_i t_{i+1} + X_i(t_{i+1} - t_{i-1})t_{i-1}t_{i+1} \\
&\quad + X_{i+1}t_i t_{i-1}(-t_i + t_{i-1}))],
\end{aligned}
\tag{B1}
$$

where $t_{\max}$ is the solution of $df(t)/dt = 0$. The found maxima, and their corresponding times, $\{t_i, X_i\}$, are then used in Eq. (9) to compute the orbit-average quantity $\bar{X}_i$, and the intermediate times, $\bar{t}_i = (t_{i+1} + t_i)/2$ [103], are associated to each $\bar{X}_i$.

As our dynamical quantity, we use p_{r_*}, but when the eccentricity $e_0 < 0.1$, we switch to $\dot{p}_{r*}$, because we find that we can reliably extract the maxima in this quantity even for very small eccentricities ($e_0 < 0.01$). This is due to the fact that the time derivative enhances the effects of the eccentric oscillations.

The orbit averaging procedure also requires the introduction of boundary conditions at the start and at the end of the inspiral.[5] At the start of the inspiral, we simply use the time of the first maximum, $t^{\text{first-max}}$. The impact of this choice is negligible because at this point of the evolution the orbit-average NQC function is quite smooth. Meanwhile, at the end of the inspiral, we need to reproduce the plunging behavior of the dynamical quantities r, ω, p_{r_*} to accurately compute the NQC function, as done in the quasicircular case. To achieve this goal, we impose that from a certain time, $t^{\text{average-end}}$, the orbit-average dynamical quantities follow the nonorbit–average dynamics. In Fig. 11, we show how the

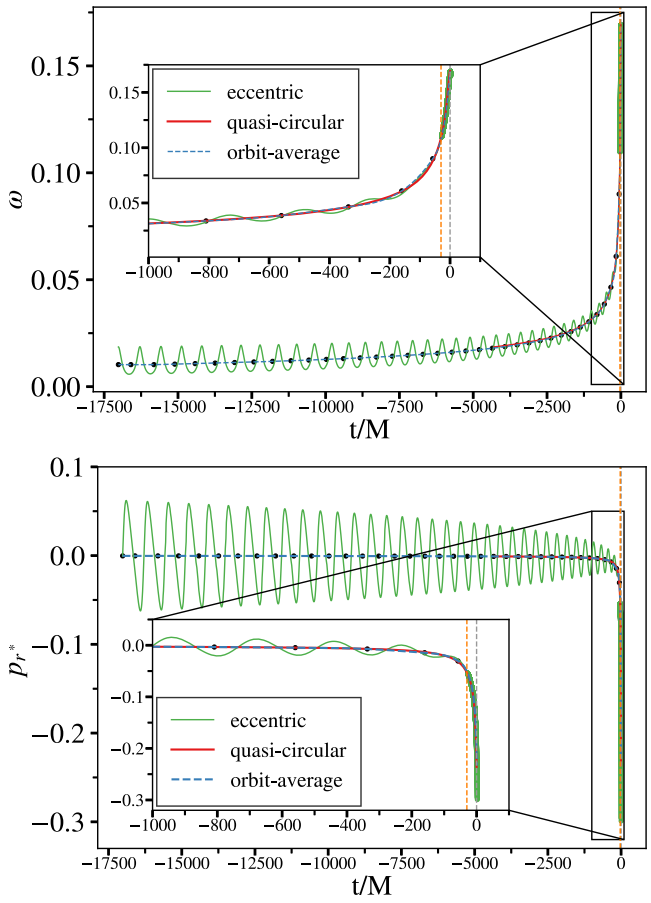

FIG. 11. Time evolution of the orbital frequency ω (upper panel), and the radial momentum p_{r*} (lower panel), for a configuration with $q = 3, \chi_1 = 0.5, \chi_2 = 0.25$. For this configuration, we show the quasicircular dynamical quantities (red solid line), the eccentric quantities with initial eccentricity $e_0 = 0.3$ (solid green line) and the orbit-average curves (blue dashed line). The black dots, on the left of the orange vertical line, represent the $\{\bar{t}_i, \bar{X}_i\}$ points used to construct the orbit-average curve, the orange vertical line represents the time $t^{\text{average-end}} = -30M$ from which the instantaneous quantities are used to construct the orbit-average curve, and the gray vertical line corresponds to time at which the inspiral ends, that is $t^{\text{inspiral-end}}$. The green dots, on the right of the vertical orange line, corresponds to values of the instantaneous eccentric quantities, which are used together with the black dots to generate the interpolated function representing the orbit-average curve. The insets in both panels zoom into the last $1000M$ of evolution to better show the behavior of the orbit-average curves at the end of the inspiral.

[5]Once an orbit-average quantity, $\{\langle t\rangle_i, \langle X\rangle_i\}$, has been computed, it is interpolated using `cubic splines` GSL routine [176] so that it can be evaluated onto the time grid with a sampling rate corresponding to the one specified by the user.

orbit-average ω and p_{r_*} are constructed from the instantaneous eccentric dynamics for a particular eccentric configuration, $q = 3, \chi_1 = 0.5, \chi_2 = 0.25, e_0 = 0.3$. Additionally, the evolution of the quasicircular quantities is included in Fig. 11, showing that the orbit-average curves for ω and p_{r_*} agree remarkably well with the ones corresponding to the quasicircular evolution.

In Fig. 11, the orange vertical line corresponds to $t^{\text{average-end}}$, from which the values of the instantaneous, eccentric dynamical variables (green dots on the right of the orange vertical line) are attached, and together with the orbit-average values (black dots on the left of the orange vertical line) form the orbit-average curve, which is then interpolated. Thus, between the time of the last found maximum, $t^{\text{last-max}}$ (the closest black dot to the orange vertical line), and the value of $t^{\text{average-end}}$ there are no points to use. If the distance between $t^{\text{last-max}}$ and $t^{\text{average-end}}$ is too large, one can get unphysical oscillations coming from interpolation artefacts due to a too large interpolated interval without points. By contrast if $t^{\text{average-end}}$ is very close to $t^{\text{last-max}}$ one could introduce residual oscillations due to eccentricity, or spurious oscillations due to the artefacts of the interpolation method, as at plunge the change of behavior of the dynamical quantities, especially p_{r^*}, challenges the interpolation procedure. Furthermore, we note that the position of $t^{\text{last-max}}$ depends substantially on the spins of the binary. For instance, for high-negative spins $t^{\text{last-max}}$ typically occurs far from the merger ($t^{\omega_{\text{peak}}} - t^{\text{last-max}} \gtrsim 100M$), while for high-positive spins $t^{\text{last-min}}$ can be very close to merger $t^{\omega_{\text{peak}}} - t^{\text{last-max}} \lesssim 50M$. We use the following phenomenological prescription for the dependence of $t^{\text{average-end}}$ with spins,

$$\begin{aligned} t_\chi^{\text{average-end}}(t_j^{\text{average-end}}, \chi_{\text{low}}, \chi_{\text{high}}, \beta_\chi; \chi_{\text{eff}}) \\ = t_0^{\text{average-end}} \times [1 - w(\beta_\chi, \chi_{\text{low}}; \chi_{\text{eff}})] \\ + t_1^{\text{average-end}} \times [1 - w(\beta_\chi, \chi_{\text{high}}; \chi_{\text{eff}})] \\ + t_2^{\text{average-end}} \times w(\beta_\chi, \chi_{\text{high}}; \chi_{\text{eff}}), \end{aligned} \tag{B2}$$

where the function w is the sigmoid defined in Eq. (8), and, the effective spin parameter is defined as,

$$\chi_{\text{eff}} = \frac{m_1 \chi_1 + m_2 \chi_2}{M}. \tag{B3}$$

In Eq. (B2) the indices takes the values $j = 0, 1, 2$, while $\beta_\chi = 50$, $\{\chi_{\text{low}}, \chi_{\text{high}}\} = \{-0.5, 0.95\}$ and $(t_0^{\text{average-end}}, t_1^{\text{average-end}}, t_2^{\text{average-end}}) = (60M, 30M, 20M)$. In Fig. 12 the dependence of $t^\chi_{\text{average-end}}$ on the effective spin parameter is illustrated. The values of the parameters $\{t_0^{\text{average-end}}, t_1^{\text{average-end}}, t_2^{\text{average-end}}, \chi_{\text{low}}, \chi_{\text{high}}\}$ are chosen after evaluating the model in a grid of points in parameter space $q = [1-20]$, $\chi_{\text{eff}} = [-0.99, 0.99]$, $e = [0, 0.3]$ with $t_{\text{append}} = [10, 100]$, and imposing that the frequency of the (2, 2)-mode does not have oscillations above 20% with respect to the (2, 2)-mode frequency of the quasicircular SEOBNRv4 model in the last 100M prior to the peak of the (2, 2)-mode amplitude. We note that the current prescription for the $t^{\text{average-end}}$ parameter is independent of the mass ratio, because we find that the spin effects are dominant for the mass ratios we consider here.

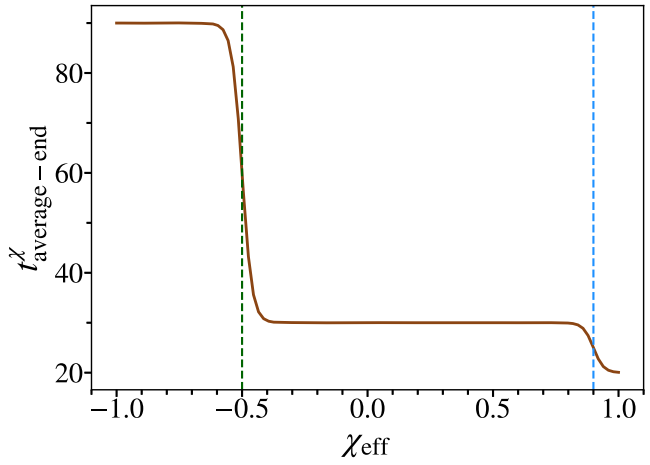

FIG. 12. Dependence of the $t_\chi^{\text{average-end}}$ parameter defined in Eq. (B3) on the effective spin parameter. The green (blue) dashed vertical line corresponds to $\chi_{\text{low}} = -0.5$ ($\chi_{\text{high}} = 0.95$) values used to construct $t_\chi^{\text{average-end}}$.

We note that the orbit averaging procedure fails when eccentricity goes to zero due to the absence of maxima in the orbital quantities, as they become nonoscillatory functions. Hence, in order to have a smooth transition to the quasicircular limit, we need a new metric to measure the distance between the time of the last found maxima, $t^{\text{last-max}}$, and the time corresponding to $t_\chi^{\text{average-end}}$. This is due to the fact that the smaller the eccentricity, the earlier $t^{\text{last-max}}$ occurs in the inspiral, and thus, the larger the region without points over which the orbit-average quantities would be interpolated. In practice, we find that one can use the time at which the inspiral ends,[6] $t^{\text{inspiral-end}}$ (dashed gray vertical line in Fig. 11), instead of $t_\chi^{\text{average-end}}$, because for low eccentricities a difference of $\sim$30–100M has negligible impact in the orbit averaging procedure. Hence, we impose that $t^{\text{average-end}}$ depends on

$$\Delta t = t^{\text{inspiral-end}} - t^{\text{last-max}}, \tag{B4}$$

such that the final expression for the $t^{\text{average-end}}$ reads as follows,

[6]We refer to the last point of the evolution of the equations of motion given by Eqs. (2).

$$t^{\text{average-end}}(\Delta t,\chi_{\text{eff}}) = t_{\chi}^{\text{average-end}}(\chi_{\text{eff}}) \times [1 - w(\beta_t, \Delta t_0; \Delta t)] + \alpha_t \times w(\beta_t, \Delta t_0; \Delta t) \times \Delta t, \tag{B5}$$

where $\beta_t = 0.1$, $\Delta t_0 = 350M$ and $\alpha_t = 0.75$. This choice of parameters ensures that $t^{\text{average-end}}$ increases as the time at which the last maximum is found occurs at earlier times in the inspiral for low-initial eccentricities, thus smoothly increasing the region in which the instantaneous variables are used to construct the orbit-average quantities. These values were set after testing and evaluating more than 10^4 waveforms for initial eccentricities $e < 0.1$ in the parameter space $q = [1, 20]$, $\chi_{\text{eff}} = [-0.9, 0.9]$. Finally, we only consider the orbit averaging procedure when at least three maxima are found during the inspiral, otherwise we use the instantaneous dynamics to construct the NQC function in Eq. (7).

APPENDIX C: PN EXPRESSIONS FOR DYNAMICAL QUANTITIES IN THE KEPLERIAN PARAMETRIZATION

In this Appendix, we provide the expressions of the dynamical quantities p_r, $\dot{p}_r$, and $\dot{r}$ in the Keplerian parametrization. They are needed for calculating the initial conditions for eccentric orbits, as discussed in Sec. II C.

In the Keplerian parametrization we have:

$$r = \frac{1}{u_p(1 + e\cos\zeta)}, \tag{C1}$$

where u_p is the inverse semilatus rectum and ζ is the relativistic anomaly. Inverting the Hamiltonian at periastron and apastron, $r_{\pm} = [u_p(1 \pm e)]^{-1}$, and solving for the energy E and u_p through to 2PN order, we obtain

$$\begin{aligned}
E =& \frac{e^2-1}{2p_\phi^2} + \frac{1-e^2}{8c^2p_\phi^4}[e^2(\nu-7)-\nu-9] + \frac{e^2-1}{16c^4p_\phi^6}[e^4(\nu^2-7\nu+33)-2e^2(\nu^2+9\nu-71)+(\nu-7)\nu+81] \\
&+ \frac{1-e^4}{c^3p_\phi^5}[2\delta\chi_A-(\nu-2)\chi_S] + \frac{1-e^2}{2c^4L^6}\{\chi_S^2[e^2(-8\nu^2+8\nu-3)-1]+\chi_A^2(3e^2+1)(4\nu-1)+2\delta\chi_A\chi_S[e^2(4\nu-3)-1]\}, \\
u_p =& \frac{1}{p_\phi^2} + \frac{e^2+3}{c^2p_\phi^4} + \frac{e^2+3}{c^4p_\phi^6}(2e^2-\nu+6) + \frac{e^2+3}{c^3p_\phi^5}[-2\delta\chi_A+(\nu-2)\chi_S] \\
&+ \frac{2}{c^4p_\phi^6}\{\chi_S^2[e^2(3\nu^2-3\nu+1)+\nu^2-\nu+1]-\chi_A^2(e^2+1)(4\nu-1)-\delta\chi_A\chi_S[e^2(3\nu-2)+\nu-2]\}.
\end{aligned} \tag{C2}$$

Inverting the Hamiltonian to obtain $p_r(E, p_\phi, r)$, then substituting Eqs. (C1) and (C2), yields $p_r(p_\phi, e, \zeta)$, which is given by the 2PN expansion

$$\begin{aligned}
p_r =& \frac{e\sin\zeta}{p_\phi} + \frac{e\sin\zeta}{c^2p_\phi^3}(e^2+e\cos\zeta+2) + \frac{e^2\sin\zeta(e-\cos\zeta)[-2\delta\chi_A+(\nu-2)\chi_S]}{c^3p_\phi^4} + \frac{e\sin\zeta}{4c^4p_\phi^5}\{8e^4+e^2(43-10\nu)-12\nu+22 \\
&+[8e^3+e(12-20\nu)]\cos\zeta+e^2(3-6\nu)\cos(2\zeta)+\chi_A^2[e^2(8\nu-2)\cos(2\zeta)+e^2(4-16\nu)+e(48\nu-12)\cos\zeta+24\nu-6] \\
&+\chi_S^2[-2e^2(1-2\nu)^2\cos(2\zeta)+e^2(8(\nu-1)\nu+4)+e(-40(\nu-1)\nu-12)\cos\zeta-6(1-2\nu)^2] \\
&-\delta\chi_A\chi_S[e^2(4-8\nu)\cos(2\zeta)+8e^2(\nu-1)+e(24-40\nu)\cos\zeta-24\nu+12]\}.
\end{aligned} \tag{C3}$$

Substituting r and p_r from Eqs. (C1) and (C3) into $\dot{p}_r = -\partial\hat{H}_{\text{EOB}}/\partial r$, and expanding yields

$$\begin{aligned}
\dot{p}_r =& \frac{e\cos\zeta(e\cos\zeta+1)^2}{p_\phi^4} - \frac{e(e\cos\zeta+1)^2[(e^2(\nu-5)-\nu-7)\cos\zeta+e(\cos(2\zeta)+3)]}{2c^2p_\phi^6} \\
&+ \frac{e(e\cos\zeta+1)^2[-2\delta\chi_A+(\nu-2)\chi_S]}{2c^3p_\phi^7}[6(e^2+1)\cos\zeta-e(3\cos(2\zeta)+1)] \\
&+ \frac{e(e\cos\zeta+1)^2}{8c^4p_\phi^8}\{2e[(e^2(\nu-7)-7\nu-41)\cos(2\zeta)+3e^2(\nu-7)-6e\nu\cos(3\zeta)+11\nu-59] \\
&+[e^4(3\nu^2-17\nu+55)-6e^2(\nu^2+3\nu-39)+3\nu^2-\nu+95]\cos\zeta\} \\
&+ \frac{e(e\cos\zeta+1)^2}{4c^4p_\phi^8}\{2\delta\chi_A\chi_S[(e^2(19-26\nu)+12\nu)\cos(\zeta)+3e^2(2\nu-1)\cos(3\zeta)+2e(11\nu-7)\cos(2\zeta)+2e(\nu-1)] \\
&+\chi_S^2[(e^2(52\nu^2-52\nu+19)-24(\nu-1)\nu)\cos(\zeta)-e(3e(1-2\nu)^2\cos(3\zeta)+2(22\nu^2-22\nu+7)\cos(2\zeta)+4\nu^2-4\nu+2)] \\
&+\chi_A^2e(4\nu-1)[-19e\cos\zeta+3e\cos(3\zeta)+14\cos(2\zeta)+2]\}.
\end{aligned} \tag{C4}$$

Similarly, for $\dot{r} = \partial \hat{H}_{\rm EOB}/\partial p_r$, we obtain

$$\begin{aligned}\dot{r} = &\frac{e\sin\zeta}{p_\phi} + \frac{e\sin\zeta}{2c^2 p_\phi^3}[e^2(-(\nu-1)) - 6e\cos\zeta + \nu - 3] + \frac{e^2\sin\zeta(\cos\zeta - e)}{c^3 p_\phi^4}[2\delta\chi_A + (2-\nu)\chi_S] \\ &+ \frac{e}{8c^4 p_\phi^5}\{2e(3e^2(\nu-3) + 11\nu - 29)\sin(2\zeta) + 3e^2(2\nu+1)\sin(3\zeta) \\ &+ [e^4(3(\nu-3)\nu + 7) + e^2(-6\nu^2 + 4\nu + 25) + 3\nu^2 + 27\nu - 81]\sin\zeta\} \\ &+ \frac{e}{2c^4 p_\phi^5}\{\chi_A^2\sin\zeta(4\nu-1)[-3e^2 + 2e\cos\zeta + 1] + \chi_S^2\sin\zeta[e^2(8\nu^2 - 8\nu + 3) - 2e(2\nu^2 - 2\nu + 1)\cos\zeta - (1-2\nu)^2] \\ &+ 2\delta\chi_A\chi_S\sin\zeta[e^2(3-4\nu) + 2e(\nu-1)\cos\zeta + 2\nu - 1]\}. \end{aligned} \tag{C5}$$

[1] H. A. Bethe and G. E. Brown, Evolution of binary compact objects which merge, Astrophys. J. **506**, 780 (1998).
[2] K. Belczynski, V. Kalogera, and T. Bulik, A comprehensive study of binary compact objects as gravitational wave sources: Evolutionary channels, rates, and physical properties, Astrophys. J. **572**, 407 (2002).
[3] M. Dominik, K. Belczynski, C. Fryer, D. E. Holz, E. Berti, T. Bulik, I. Mandel, and R. O'Shaughnessy, Double compact objects II: Cosmological merger rates, Astrophys. J. **779**, 72 (2013).
[4] K. Belczynski, A. Buonanno, M. Cantiello, C. L. Fryer, D. E. Holz, I. Mandel, M. C. Miller, and M. Walczak, The formation and gravitational-wave detection of massive stellar black-hole binaries, Astrophys. J. **789**, 120 (2014).
[5] N. Mennekens and D. Vanbeveren, Massive double compact object mergers: Gravitational wave sources and r-process element production sites, Astron. Astrophys. **564**, A134 (2014).
[6] M. Spera, M. Mapelli, and A. Bressan, The mass spectrum of compact remnants from the parsec stellar evolution tracks, Mon. Not. R. Astron. Soc. **451**, 4086 (2015).
[7] K. Belczynski, D. E. Holz, T. Bulik, and R. O'Shaughnessy, The first gravitational-wave source from the isolated evolution of two 40–100 Msun stars, Nature (London) **534**, 512 (2016).
[8] J. J. Eldridge and E. R. Stanway, BPASS predictions for binary black-hole mergers, Mon. Not. R. Astron. Soc. **462**, 3302 (2016).
[9] P. Marchant, N. Langer, P. Podsiadlowski, T. M. Tauris, and T. J. Moriya, A new route towards merging massive black holes, Astron. Astrophys. **588**, A50 (2016).
[10] M. Mapelli, N. Giacobbo, E. Ripamonti, and M. Spera, The cosmic merger rate of stellar black hole binaries from the Illustris simulation, Mon. Not. R. Astron. Soc. **472**, 2422 (2017).
[11] M. Mapelli and N. Giacobbo, The cosmic merger rate of neutron stars and black holes, Mon. Not. R. Astron. Soc. **479**, 4391 (2018).
[12] S. Stevenson, A. Vigna-Gómez, I. Mandel, J. W. Barrett, C. J. Neijssel, D. Perkins, and S. E. de Mink, Formation of the first three gravitational-wave observations through isolated binary evolution, Nat. Commun. **8**, 14906 (2017).
[13] N. Giacobbo and M. Mapelli, The progenitors of compact-object binaries: Impact of metallicity, common envelope and natal kicks, Mon. Not. R. Astron. Soc. **480**, 2011 (2018).
[14] M. U. Kruckow, T. M. Tauris, N. Langer, M. Kramer, and R. G. Izzard, Progenitors of gravitational wave mergers: Binary evolution with the stellar grid-based code ComBinE, Mon. Not. R. Astron. Soc. **481**, 1908 (2018).
[15] P. C. Peters, Gravitational radiation and the motion of two point masses, Phys. Rev. **136**, B1224 (1964).
[16] J. Aasi *et al.* (LIGO Scientific Collaboration), Advanced LIGO, Classical Quant. Grav. **32**, 115012 (2015).
[17] F. Acernese *et al.* (VIRGO Collaboration), Advanced Virgo: A second-generation interferometric gravitational wave detector, Classical Quant. Grav. **32**, 024001 (2015).
[18] T. Akutsu *et al.* (KAGRA Collaboration), KAGRA: 2.5 generation interferometric gravitational wave detector, Nat. Astron. **3**, 35 (2019).
[19] S. F. P. Zwart and S. McMillan, Black hole mergers in the universe, Astrophys. J. Lett. **528**, L17 (2000).
[20] M. C. Miller and D. P. Hamilton, Production of intermediate-mass black holes in globular clusters, Mon. Not. R. Astron. Soc. **330**, 232 (2002).
[21] M. C. Miller and D. P. Hamilton, Four-body effects in globular cluster black hole coalescence, Astrophys. J. **576**, 894 (2002).
[22] K. Gultekin, M. C. Miller, and D. P. Hamilton, Growth of intermediate–mass black holes in globular clusters, Astrophys. J. **616**, 221 (2004).
[23] K. Gultekin, M. C. Miller, and D. P. Hamilton, Three-body dynamics with gravitational wave emission, Astrophys. J. **640**, 156 (2006).
[24] R. M. O'Leary, F. A. Rasio, J. M. Fregeau, N. Ivanova, and R. W. O'Shaughnessy, Binary mergers and growth of black holes in dense star clusters, Astrophys. J. **637**, 937 (2006).
[25] A. Sadowski, K. Belczynski, T. Bulik, N. Ivanova, F. A. Rasio, and R. W. O'Shaughnessy, The total merger rate of compact object binaries in the local Universe, Astrophys. J. **676**, 1162 (2008).

[26] J. M. B. Downing, M. J. Benacquista, M. Giersz, and R. Spurzem, Compact binaries in star clusters–i. Black hole binaries inside globular clusters, Mon. Not. R. Astron. Soc. **407**, 1946 (2010).
[27] J. M. B. Downing, M. J. Benacquista, M. Giersz, and R. Spurzem, Compact binaries in star clusters–ii. Escapers and detection rates, Mon. Not. R. Astron. Soc. **416**, 133 (2011).
[28] J. Samsing, M. MacLeod, and E. Ramirez-Ruiz, The formation of eccentric compact binary inspirals and the role of gravitational wave emission in binary-single stellar encounters, Astrophys. J. **784**, 71 (2014).
[29] C. L. Rodriguez, M. Morscher, B. Pattabiraman, S. Chatterjee, C.-J. Haster, and F. A. Rasio, Binary Black Hole Mergers from Globular Clusters: Implications for Advanced LIGO, Phys. Rev. Lett. **115**, 051101 (2015); Erratum, Phys. Rev. Lett. **116**, 029901 (2016).
[30] A. Askar, M. Szkudlarek, D. Gondek-Rosińska, M. Giersz, and T. Bulik, MOCCA-SURVEY Database–I. Coalescing binary black holes originating from globular clusters, Mon. Not. R. Astron. Soc. **464**, L36 (2017).
[31] C. L. Rodriguez, S. Chatterjee, and F. A. Rasio, Binary black hole mergers from globular clusters: Masses, merger rates, and the impact of stellar evolution, Phys. Rev. D **93**, 084029 (2016).
[32] C. L. Rodriguez, C.-J. Haster, S. Chatterjee, V. Kalogera, and F. A. Rasio, Dynamical formation of the GW150914 binary black hole, Astrophys. J. Lett. **824**, L8 (2016).
[33] J. Samsing and E. Ramirez-Ruiz, On the assembly rate of highly eccentric binary black hole mergers, Astrophys. J. Lett. **840**, L14 (2017).
[34] J. Samsing, Eccentric black hole mergers forming in globular clusters, Phys. Rev. D **97**, 103014 (2018).
[35] C. L. Rodriguez, P. Amaro-Seoane, S. Chatterjee, and F. A. Rasio, Post-Newtonian Dynamics in Dense Star Clusters: Highly-Eccentric, Highly-Spinning, and Repeated Binary Black Hole Mergers, Phys. Rev. Lett. **120**, 151101 (2018).
[36] C. L. Rodriguez and A. Loeb, Redshift Evolution of the Black Hole Merger Rate from Globular Clusters, Astrophys. J. Lett. **866**, L5 (2018).
[37] G. Fragione and B. Kocsis, Black Hole Mergers from an Evolving Population of Globular Clusters, Phys. Rev. Lett. **121**, 161103 (2018).
[38] M. Zevin, J. Samsing, C. Rodriguez, C.-J. Haster, and E. Ramirez-Ruiz, Eccentric black hole mergers in dense star clusters: The role of binary–binary encounters, Astrophys. J. **871**, 91 (2019).
[39] L. Gondán and B. Kocsis, High eccentricities and high masses characterize gravitational-wave captures in galactic nuclei as seen by Earth-based detectors, Mon. Not. R. Astron. Soc. **506**, 1665 (2021).
[40] R. M. O'Leary, B. Kocsis, and A. Loeb, Gravitational waves from scattering of stellar-mass black holes in galactic nuclei, Mon. Not. R. Astron. Soc. **395**, 2127 (2009).
[41] F. Antonini and H. B. Perets, Secular evolution of compact binaries near massive black holes: Gravitational wave sources and other exotica, Astrophys. J. **757**, 27 (2012).
[42] D. Tsang, Shattering flares during close encounters of neutron stars, Astrophys. J. **777**, 103 (2013).
[43] F. Antonini and F. A. Rasio, Merging black hole binaries in galactic nuclei: Implications for Advanced-LIGO detections, Astrophys. J. **831**, 187 (2016).
[44] C. Petrovich and F. Antonini, Greatly enhanced merger rates of compact-object binaries in non-spherical nuclear star clusters, Astrophys. J. **846**, 146 (2017).
[45] N. C. Stone, B. D. Metzger, and Z. Haiman, Assisted inspirals of stellar mass black holes embedded in AGN discs: Solving the "final AU problem", Mon. Not. R. Astron. Soc. **464**, 946 (2017).
[46] N. C. Stone, A. H. W. Küpper, and J. P. Ostriker, Formation of massive black holes in galactic nuclei: Runaway tidal encounters, Mon. Not. R. Astron. Soc. **467**, 4180 (2017).
[47] A. Rasskazov and B. Kocsis, The rate of stellar mass black hole scattering in galactic nuclei, Astrophys. J. **881**, 20 (2019).
[48] Y. Kozai, Secular perturbations of asteroids with high inclination and eccentricity, Astron. J. **67**, 591 (1962).
[49] M. L. Lidov, The evolution of orbits of artificial satellites of planets under the action of gravitational perturbations of external bodies, AIAA J. **9**, 719 (1962).
[50] L. Wen, On the eccentricity distribution of coalescing black hole binaries driven by the Kozai mechanism in globular clusters, Astrophys. J. **598**, 419 (2003).
[51] J. H. VanLandingham, M. C. Miller, D. P. Hamilton, and D. C. Richardson, The role of the Kozai–Lidov mechanism in black hole binary mergers in galactic centers, Astrophys. J. **828**, 77 (2016).
[52] C. L. Rodriguez, M. Zevin, C. Pankow, V. Kalogera, and F. A. Rasio, Illuminating black hole binary formation channels with spins in Advanced LIGO, Astrophys. J. Lett. **832**, L2 (2016).
[53] F. Antonini, S. Toonen, and A. S. Hamers, Binary black hole mergers from field triples: Properties, rates and the impact of stellar evolution, Astrophys. J. **841**, 77 (2017).
[54] G. Fragione and O. Bromberg, Eccentric binary black hole mergers in globular clusters hosting intermediate-mass black holes, Mon. Not. R. Astron. Soc. **488**, 4370 (2019).
[55] G. Fragione, E. Grishin, N. W. C. Leigh, H. B. Perets, and R. Perna, Black hole and neutron star mergers in galactic nuclei, Mon. Not. R. Astron. Soc. **488**, 47 (2019).
[56] G. Fragione and B. Kocsis, Black hole mergers from quadruples, Mon. Not. R. Astron. Soc. **486**, 4781 (2019).
[57] I. Mandel and R. O'Shaughnessy, Compact binary coalescences in the band of ground-based gravitational-wave detectors, Classical Quant. Grav. **27**, 114007 (2010).
[58] B. P. Abbott *et al.* (LIGO Scientific and Virgo Collaborations), Astrophysical implications of the binary black-hole merger GW150914, Astrophys. J. Lett. **818**, L22 (2016).
[59] W. M. Farr, S. Stevenson, M. C. Miller, I. Mandel, B. Farr, and A. Vecchio, Distinguishing spin-aligned and isotropic black hole populations with gravitational waves, Nature (London) **548**, 426 (2017).
[60] B. P. Abbott *et al.* (LIGO Scientific and Virgo Collaborations), Binary black hole population properties inferred from the first and second observing runs of Advanced LIGO and Advanced Virgo, Astrophys. J. Lett. **882**, L24 (2019).
[61] M. Zevin, I. M. Romero-Shaw, K. Kremer, E. Thrane, and P. D. Lasky, Implications of eccentric observations on

binary black hole formation channels, Astrophys. J. Lett. **921**, L43 (2021).
[62] LIGO Scientific, Virgo, and KAGRA Collaborations, The population of merging compact binaries inferred using gravitational waves through GWTC-3, arXiv:2111.03634.
[63] B. P. Abbott *et al.* (LIGO Scientific and Virgo Collaborations), GWTC-1: A Gravitational-Wave Transient Catalog of Compact Binary Mergers Observed by LIGO and Virgo during the First and Second Observing Runs, Phys. Rev. X **9**, 031040 (2019).
[64] R. Abbott *et al.* (LIGO Scientific and Virgo Collaborations), GWTC-2: Compact Binary Coalescences Observed by LIGO and Virgo During the First Half of the Third Observing Run, Phys. Rev. X **11**, 021053 (2021).
[65] R. Abbott *et al.* (LIGO Scientific, VIRGO, and KAGRA Collaborations), GWTC-3: Compact binary coalescences observed by LIGO and Virgo during the second part of the third observing run, arXiv:2111.03606.
[66] B. P. Abbott *et al.* (LIGO Scientific and Virgo Collaborations), Search for eccentric binary black hole mergers with Advanced LIGO and Advanced Virgo during their first and second observing runs, Astrophys. J. **883**, 149 (2019).
[67] I. M. Romero-Shaw, P. D. Lasky, and E. Thrane, Searching for eccentricity: Signatures of dynamical formation in the first gravitational-wave transient catalogue of LIGO and Virgo, Mon. Not. R. Astron. Soc. **490**, 5210 (2019).
[68] A. H. Nitz, A. Lenon, and D. A. Brown, Search for eccentric binary neutron star mergers in the first and second observing runs of Advanced LIGO, Astrophys. J. **890**, 1 (2020).
[69] I. M. Romero-Shaw, P. D. Lasky, E. Thrane, and J. C. Bustillo, GW190521: Orbital eccentricity and signatures of dynamical formation in a binary black hole merger signal, Astrophys. J. Lett. **903**, L5 (2020).
[70] V. Gayathri, J. Healy, J. Lange, B. O'Brien, M. Szczepanczyk, I. Bartos, M. Campanelli, S. Klimenko, C. Lousto, and R. O'Shaughnessy, GW190521 as a highly eccentric black hole merger, arXiv:2009.05461.
[71] M. Favata, C. Kim, K. G. Arun, J. C. Kim, and H. W. Lee, Constraining the orbital eccentricity of inspiralling compact binary systems with Advanced LIGO, arXiv:2108.05861 [Phys. Rev. D (to be published)].
[72] E. O'Shea and P. Kumar, Correlations in parameter estimation of low-mass eccentric binaries: GW151226 & GW170608, arXiv:2107.07981.
[73] I. M. Romero-Shaw, P. D. Lasky, and E. Thrane, Signs of eccentricity in two gravitational-wave signals may indicate a sub-population of dynamically assembled binary black holes, Astrophys. J. Lett. **921**, L31 (2021).
[74] M. Punturo *et al.*, The Einstein Telescope: A third-generation gravitational wave observatory, Classical Quant. Grav. **27**, 194002 (2010).
[75] B. P. Abbott *et al.* (LIGO Scientific Collaboration), Exploring the sensitivity of next generation gravitational wave detectors, Classical Quant. Grav. **34**, 044001 (2017).
[76] D. Reitze *et al.*, The US Program in ground-based gravitational wave science: Contribution from the LIGO Laboratory, Bull. Am. Astron. Soc. **51**, 141 (2019).
[77] D. Reitze *et al.*, Cosmic explorer: The U.S. contribution to gravitational-wave astronomy beyond LIGO, Bull. Am. Astron. Soc. **51**, 035 (2019).
[78] P. Amaro-Seoane *et al.*, Laser interferometer space antenna, arXiv:1702.00786.
[79] J. Luo *et al.* (TianQin Collaboration), TianQin: A space-borne gravitational wave detector, Classical Quant. Grav. **33**, 035010 (2016).
[80] A. Sesana, Self consistent model for the evolution of eccentric massive black hole binaries in stellar environments: Implications for gravitational wave observations, Astrophys. J. **719**, 851 (2010).
[81] K. Breivik, C. L. Rodriguez, S. L. Larson, V. Kalogera, and F. A. Rasio, Distinguishing between formation channels for binary black holes with LISA, Astrophys. J. Lett. **830**, L18 (2016).
[82] J. Samsing and D. J. D'Orazio, Black hole mergers from globular clusters observable by LISA I: Eccentric sources originating from relativistic *N*-body dynamics, Mon. Not. R. Astron. Soc. **481**, 5445 (2018).
[83] V. Cardoso, C. F. B. Macedo, and R. Vicente, Eccentricity evolution of compact binaries and applications to gravitational-wave physics, Phys. Rev. D **103**, 023015 (2021).
[84] A. Gopakumar and B. R. Iyer, Gravitational waves from inspiralling compact binaries: Angular momentum flux, evolution of the orbital elements and the wave form to the second post-Newtonian order, Phys. Rev. D **56**, 7708 (1997).
[85] A. Gopakumar and B. R. Iyer, Second post-Newtonian gravitational wave polarizations for compact binaries in elliptical orbits, Phys. Rev. D **65**, 084011 (2002).
[86] T. Damour, A. Gopakumar, and B. R. Iyer, Phasing of gravitational waves from inspiralling eccentric binaries, Phys. Rev. D **70**, 064028 (2004).
[87] C. Konigsdorffer and A. Gopakumar, Phasing of gravitational waves from inspiralling eccentric binaries at the third-and-a-half post-Newtonian order, Phys. Rev. D **73**, 124012 (2006).
[88] K. G. Arun, L. Blanchet, B. R. Iyer, and M. S. S. Qusailah, Tail effects in the 3PN gravitational wave energy flux of compact binaries in quasielliptical orbits, Phys. Rev. D **77**, 064034 (2008).
[89] K. G. Arun, L. Blanchet, B. R. Iyer, and M. S. S. Qusailah, Inspiralling compact binaries in quasielliptical orbits: The complete 3PN energy flux, Phys. Rev. D **77**, 064035 (2008).
[90] K. G. Arun, L. Blanchet, B. R. Iyer, and S. Sinha, Third post-Newtonian angular momentum flux and the secular evolution of orbital elements for inspiralling compact binaries in quasi-elliptical orbits, Phys. Rev. D **80**, 124018 (2009).
[91] R.-M. Memmesheimer, A. Gopakumar, and G. Schaefer, Third post-Newtonian accurate generalized quasi-Keplerian parametrization for compact binaries in eccentric orbits, Phys. Rev. D **70**, 104011 (2004).
[92] N. Yunes, K. G. Arun, E. Berti, and C. M. Will, Post-circular expansion of eccentric binary inspirals: Fourier-domain waveforms in the stationary phase approximation, Phys. Rev. D **80**, 084001 (2009); Erratum, Phys. Rev. D **89**, 109901 (2014).
[93] E. A. Huerta, P. Kumar, S. T. McWilliams, R. O'Shaughnessy, and N. Yunes, Accurate and efficient waveforms for compact binaries on eccentric orbits, Phys. Rev. D **90**, 084016 (2014).

[94] C. K. Mishra, K. G. Arun, and B. R. Iyer, Third post-Newtonian gravitational waveforms for compact binary systems in general orbits: Instantaneous terms, Phys. Rev. D **91**, 084040 (2015).
[95] N. Loutrel and N. Yunes, Eccentric gravitational wave bursts in the post-Newtonian formalism, Classical Quant. Grav. **34**, 135011 (2017).
[96] A. Klein, Y. Boetzel, A. Gopakumar, P. Jetzer, and L. de Vittori, Fourier domain gravitational waveforms for precessing eccentric binaries, Phys. Rev. D **98**, 104043 (2018).
[97] B. Moore, T. Robson, N. Loutrel, and N. Yunes, Towards a Fourier domain waveform for non-spinning binaries with arbitrary eccentricity, Classical Quant. Grav. **35**, 235006 (2018).
[98] B. Moore and N. Yunes, A 3PN Fourier domain waveform for non-spinning binaries with moderate eccentricity, Classical Quant. Grav. **36**, 185003 (2019).
[99] S. Tanay, A. Klein, E. Berti, and A. Nishizawa, Convergence of Fourier-domain templates for inspiraling eccentric compact binaries, Phys. Rev. D **100**, 064006 (2019).
[100] S. Tiwari and A. Gopakumar, Combining post-circular and Padé approximations to compute Fourier domain templates for eccentric inspirals, Phys. Rev. D **102**, 084042 (2020).
[101] I. Hinder, F. Herrmann, P. Laguna, and D. Shoemaker, Comparisons of eccentric binary black hole simulations with post-Newtonian models, Phys. Rev. D **82**, 024033 (2010).
[102] E. A. Huerta *et al.*, Physics of eccentric binary black hole mergers: A numerical relativity perspective, Phys. Rev. D **100**, 064003 (2019).
[103] A. G. M. Lewis, A. Zimmerman, and H. P. Pfeiffer, Fundamental frequencies and resonances from eccentric and precessing binary black hole inspirals, Classical Quant. Grav. **34**, 124001 (2017).
[104] S. Habib and E. A. Huerta, Characterization of numerical relativity waveforms of eccentric binary black hole mergers, Phys. Rev. D **100**, 044016 (2019).
[105] A. Ramos-Buades, S. Husa, G. Pratten, H. Estellés, C. García-Quirós, M. Mateu-Lucena, M. Colleoni, and R. Jaume, First survey of spinning eccentric black hole mergers: Numerical relativity simulations, hybrid waveforms, and parameter estimation, Phys. Rev. D **101**, 083015 (2020).
[106] T. Islam, V. Varma, J. Lodman, S. E. Field, G. Khanna, M. A. Scheel, H. P. Pfeiffer, D. Gerosa, and L. E. Kidder, Eccentric binary black hole surrogate models for the gravitational waveform and remnant properties: Comparable mass, nonspinning case, Phys. Rev. D **103**, 064022 (2021).
[107] I. Hinder, L. E. Kidder, and H. P. Pfeiffer, Eccentric binary black hole inspiral-merger-ringdown gravitational waveform model from numerical relativity and post-Newtonian theory, Phys. Rev. D **98**, 044015 (2018).
[108] E. A. Huerta *et al.*, Eccentric, nonspinning, inspiral, Gaussian-process merger approximant for the detection and characterization of eccentric binary black hole mergers, Phys. Rev. D **97**, 024031 (2018).
[109] Y. Setyawati and F. Ohme, Adding eccentricity to quasi-circular binary-black-hole waveform models, Phys. Rev. D **103**, 124011 (2021).
[110] R. Gold, S. Bernuzzi, M. Thierfelder, B. Brugmann, and F. Pretorius, Eccentric binary neutron star mergers, Phys. Rev. D **86**, 121501 (2012).
[111] W. E. East, F. Pretorius, and B. C. Stephens, Eccentric black hole-neutron star mergers: Effects of black hole spin and equation of state, Phys. Rev. D **85**, 124009 (2012).
[112] H. Yang, W. E. East, V. Paschalidis, F. Pretorius, and R. F. P. Mendes, Evolution of highly eccentric binary neutron stars including tidal effects, Phys. Rev. D **98**, 044007 (2018).
[113] C. Chirenti, R. Gold, and M. C. Miller, Gravitational waves from f-modes excited by the inspiral of highly eccentric neutron star binaries, Astrophys. J. **837**, 67 (2017).
[114] J. Samsing, M. MacLeod, and E. Ramirez-Ruiz, Formation of tidal captures and gravitational wave inspirals in binary-single interactions, Astrophys. J. **846**, 36 (2017).
[115] H. Yang, Inspiralling eccentric binary neutron stars: Orbital motion and tidal resonance, Phys. Rev. D **100**, 064023 (2019).
[116] A. Buonanno and T. Damour, Effective one-body approach to general relativistic two-body dynamics, Phys. Rev. D **59**, 084006 (1999).
[117] A. Buonanno and T. Damour, Transition from inspiral to plunge in binary black hole coalescences, Phys. Rev. D **62**, 064015 (2000).
[118] T. Hinderer and S. Babak, Foundations of an effective-one-body model for coalescing binaries on eccentric orbits, Phys. Rev. D **96**, 104048 (2017).
[119] Z. Cao and W.-B. Han, Waveform model for an eccentric binary black hole based on the effective-one-body-numerical-relativity formalism, Phys. Rev. D **96**, 044028 (2017).
[120] X. Liu, Z. Cao, and L. Shao, Validating the effective-one-body numerical-relativity waveform models for spin-aligned binary black holes along eccentric orbits, Phys. Rev. D **101**, 044049 (2020).
[121] D. Chiaramello and A. Nagar, Faithful analytical effective-one-body waveform model for spin-aligned, moderately eccentric, coalescing black hole binaries, Phys. Rev. D **101**, 101501 (2020).
[122] X. Liu, Z. Cao, and Z.-H. Zhu, A higher-multipole gravitational waveform model for an eccentric binary black holes based on the effective-one-body-numerical-relativity formalism, arXiv:2102.08614.
[123] A. Nagar, A. Bonino, and P. Rettegno, Effective one-body multipolar waveform model for spin-aligned, quasicircular, eccentric, hyperbolic black hole binaries, Phys. Rev. D **103**, 104021 (2021).
[124] A. Nagar and P. Rettegno, Next generation: Impact of high-order analytical information on effective one body waveform models for noncircularized, spin-aligned black hole binaries, Phys. Rev. D **104**, 104004 (2021).
[125] S. Albanesi, A. Nagar, and S. Bernuzzi, Effective one-body model for extreme-mass-ratio spinning binaries on eccentric equatorial orbits: Testing radiation reaction and waveform, Phys. Rev. D **104**, 024067 (2021).
[126] M. Khalil, A. Buonanno, J. Steinhoff, and J. Vines, Radiation-reaction force and multipolar waveforms for

eccentric, spin-aligned binaries in the effective-one-body formalism, Phys. Rev. D **104**, 024046 (2021).
[127] A. Placidi, S. Albanesi, A. Nagar, M. Orselli, S. Bernuzzi, and G. Grignani, Exploiting Newton-factorized, 2PN-accurate, waveform multipoles in effective-one-body models for spin-aligned noncircularized binaries, arXiv:2112.05448.
[128] T. Damour, B. R. Iyer, and A. Nagar, Improved resummation of post-Newtonian multipolar waveforms from circularized compact binaries, Phys. Rev. D **79**, 064004 (2009).
[129] Y. Pan, A. Buonanno, R. Fujita, E. Racine, and H. Tagoshi, Post-Newtonian factorized multipolar waveforms for spinning, non-precessing black-hole binaries, Phys. Rev. D **83**, 064003 (2011); Erratum, Phys. Rev. D **87**, 109901 (2013).
[130] Y. Pan, A. Buonanno, A. Taracchini, L. E. Kidder, A. H. Mroué, H. P. Pfeiffer, M. A. Scheel, and B. Szilágyi, Inspiral-merger-ringdown waveforms of spinning, precessing black-hole binaries in the effective-one-body formalism, Phys. Rev. D **89**, 084006 (2014).
[131] A. Taracchini *et al.*, Effective-one-body model for black-hole binaries with generic mass ratios and spins, Phys. Rev. D **89**, 061502 (2014).
[132] A. Bohé *et al.*, Improved effective-one-body model of spinning, nonprecessing binary black holes for the era of gravitational-wave astrophysics with advanced detectors, Phys. Rev. D **95**, 044028 (2017).
[133] A. Nagar *et al.*, Time-domain effective-one-body gravitational waveforms for coalescing compact binaries with nonprecessing spins, tides and self-spin effects, Phys. Rev. D **98**, 104052 (2018).
[134] R. Cotesta, A. Buonanno, A. Bohé, A. Taracchini, I. Hinder, and S. Ossokine, Enriching the symphony of gravitational waves from binary black holes by tuning higher harmonics, Phys. Rev. D **98**, 084028 (2018).
[135] S. Babak, A. Taracchini, and A. Buonanno, Validating the effective-one-body model of spinning, precessing binary black holes against numerical relativity, Phys. Rev. D **95**, 024010 (2017).
[136] A. Nagar and P. Rettegno, Efficient effective one body time-domain gravitational waveforms, Phys. Rev. D **99**, 021501 (2019).
[137] S. Ossokine *et al.*, Multipolar effective-one-body waveforms for precessing binary black holes: Construction and validation, Phys. Rev. D **102**, 044055 (2020).
[138] G. Riemenschneider, P. Rettegno, M. Breschi, A. Albertini, R. Gamba, S. Bernuzzi, and A. Nagar, Assessment of consistent next-to-quasicircular corrections and postadiabatic approximation in effective-one-body multipolar waveforms for binary black hole coalescences, Phys. Rev. D **104**, 104045 (2021).
[139] D. P. Mihaylov, S. Ossokine, A. Buonanno, and A. Ghosh, Fast post-adiabatic waveforms in the time domain: Applications to compact binary coalescences in LIGO and Virgo, arXiv:2105.06983 [Phys. Rev. D (to be published)].
[140] R. Gamba, S. Akçay, S. Bernuzzi, and J. Williams, Effective-one-body waveforms for precessing coalescing compact binaries with post-Newtonian twist, arXiv:2111.03675.
[141] M. Boyle *et al.*, The SXS collaboration catalog of binary black hole simulations, Classical Quant. Grav. **36**, 195006 (2019).
[142] The SXS binary black hole simulations catalog, https://data.black-holes.org/waveforms.
[143] E. Barausse and A. Buonanno, Extending the effective-one-body Hamiltonian of black-hole binaries to include next-to-next-to-leading spin-orbit couplings, Phys. Rev. D **84**, 104027 (2011).
[144] Y. Pan, A. Buonanno, M. Boyle, L. T. Buchman, L. E. Kidder, H. P. Pfeiffer, and M. A. Scheel, Inspiral-merger-ringdown multipolar waveforms of nonspinning black-hole binaries using the effective-one-body formalism, Phys. Rev. D **84**, 124052 (2011).
[145] A. Buonanno, Y. Chen, and T. Damour, Transition from inspiral to plunge in precessing binaries of spinning black holes, Phys. Rev. D **74**, 104005 (2006).
[146] S. Ossokine *et al.* (to be published).
[147] A. Taracchini, Y. Pan, A. Buonanno, E. Barausse, M. Boyle, T. Chu, G. Lovelace, H. P. Pfeiffer, and M. A. Scheel, Prototype effective-one-body model for nonprecessing spinning inspiral-merger-ringdown waveforms, Phys. Rev. D **86**, 024011 (2012).
[148] T. Mora and C. M. Will, Numerically generated quasiequilibrium orbits of black holes: Circular or eccentric?, Phys. Rev. D **66**, 101501 (2002).
[149] A. Ramos-Buades (to be published).
[150] T. Damour, F. Guercilena, I. Hinder, S. Hopper, A. Nagar, and L. Rezzolla, Strong-field scattering of two black holes: Numerics versus analytics, Phys. Rev. D **89**, 081503 (2014).
[151] A. Nagar, P. Rettegno, R. Gamba, and S. Bernuzzi, Effective-one-body waveforms from dynamical captures in black hole binaries, Phys. Rev. D **103**, 064013 (2021).
[152] R. Gamba, M. Breschi, G. Carullo, P. Rettegno, S. Albanesi, S. Bernuzzi, and A. Nagar, GW190521: A dynamical capture of two black holes, arXiv:2106.05575.
[153] D. Bini, A. Geralico, and J. Vines, Hyperbolic scattering of spinning particles by a Kerr black hole, Phys. Rev. D **96**, 084044 (2017).
[154] G. Cho, A. Gopakumar, M. Haney, and H. M. Lee, Gravitational waves from compact binaries in post-Newtonian accurate hyperbolic orbits, Phys. Rev. D **98**, 024039 (2018).
[155] S. Mukherjee, S. Mitra, and S. Chatterjee, Gravitational wave observatories may be able to detect hyperbolic encounters of black holes, Mon. Not. R. Astron. Soc. **508**, 5064 (2021).
[156] B. S. Sathyaprakash and S. V. Dhurandhar, Choice of filters for the detection of gravitational waves from coalescing binaries, Phys. Rev. D **44**, 3819 (1991).
[157] L. S. Finn and D. F. Chernoff, Observing binary inspiral in gravitational radiation: One interferometer, Phys. Rev. D **47**, 2198 (1993).
[158] L. Barsotti, P. Fritschel, M. Evans, and S. Gras (LIGO Collaboration), Updated advanced ligo sensitivity design curve, LIGO Document T1800044-v5, 2018.
[159] C. García-Quirós, M. Colleoni, S. Husa, H. Estellés, G. Pratten, A. Ramos-Buades, M. Mateu-Lucena, and R. Jaume, Multimode frequency-domain model for the gravi-

tational wave signal from nonprecessing black-hole binaries, Phys. Rev. D **102**, 064002 (2020).
[160] https://www.black-holes.org/SpEC.html.
[161] C. Capano, Y. Pan, and A. Buonanno, Impact of higher harmonics in searching for gravitational waves from nonspinning binary black holes, Phys. Rev. D **89**, 102003 (2014).
[162] B. Allen, W. G. Anderson, P. R. Brady, D. A. Brown, and J. D. E. Creighton, FINDCHIRP: An algorithm for detection of gravitational waves from inspiraling compact binaries, Phys. Rev. D **85**, 122006 (2012).
[163] A. Nitz *et al.*, gwastro/pycbc: Pycbc release v1.15.4 (2020), 10.5281/zenodo.5825666.
[164] The LIGO Scientific Collaboration, Lalsuite: LSC Algorithm Library Suite, https://www.lsc-group.phys.uwm.edu/daswg/projects/lalsuite.html (2015).
[165] K. Martel and E. Poisson, Gravitational waves from eccentric compact binaries: Reduction in signal-to-noise ratio due to nonoptimal signal processing, Phys. Rev. D **60**, 124008 (1999).
[166] E. A. Huerta and D. A. Brown, Effect of eccentricity on binary neutron star searches in Advanced LIGO, Phys. Rev. D **87**, 127501 (2013).
[167] A. Ramos-Buades, S. Tiwari, M. Haney, and S. Husa, Impact of eccentricity on the gravitational wave searches for binary black holes: High mass case, Phys. Rev. D **102**, 043005 (2020).
[168] A. H. Nitz and Y.-F. Wang, Search for gravitational waves from the coalescence of subsolar mass and eccentric compact binaries, Astrophys. J. **915**, 54 (2021).
[169] A. K. Lenon, D. A. Brown, and A. H. Nitz, Eccentric binary neutron star search prospects for cosmic explorer, Phys. Rev. D **104**, 063011 (2021).
[170] S. Privitera, S. R. P. Mohapatra, P. Ajith, K. Cannon, N. Fotopoulos, M. A. Frei, C. Hanna, A. J. Weinstein, and J. T. Whelan, Improving the sensitivity of a search for coalescing binary black holes with nonprecessing spins in gravitational wave data, Phys. Rev. D **89**, 024003 (2014).
[171] S. A. Usman *et al.*, The PyCBC search for gravitational waves from compact binary coalescence, Classical Quant. Grav. **33**, 215004 (2016).
[172] C. Messick, K. Blackburn, P. Brady, P. Brockill, K. Cannon, R. Cariou, S. Caudill, S. J. Chamberlin, J. D. E. Creighton, R. Everett *et al.*, Analysis framework for the prompt discovery of compact binary mergers in gravitational-wave data, Phys. Rev. D **95**, 042001 (2017).
[173] I. Hinder, B. Vaishnav, F. Herrmann, D. Shoemaker, and P. Laguna, Universality and final spin in eccentric binary black hole inspirals, Phys. Rev. D **77**, 081502 (2008).
[174] M. Pürrer, Frequency domain reduced order models for gravitational waves from aligned-spin compact binaries, Classical Quant. Grav. **31**, 195010 (2014).
[175] Q. Yun, W.-B. Han, X. Zhong, and C. A. Benavides-Gallego, Surrogate model for gravitational waveforms of spin-aligned binary black holes with eccentricities, Phys. Rev. D **103**, 124053 (2021).
[176] M. Galassi *et al.*, GNU Scientific Library Reference Manual, 3rd ed. (2018), http://www.gnu.org/software/gsl/.